SIAM J. SCI. COMPUT.
Vol. 41, No. 6, pp. B1178–B1210

A MASS-CONSERVATIVE TEMPORAL SECOND ORDER AND SPATIAL FOURTH ORDER CHARACTERISTIC FINITE VOLUME METHOD FOR ATMOSPHERIC POLLUTION ADVECTION DIFFUSION PROBLEMS*

KAI FU† AND DONG LIANG‡

Abstract. In this paper, a mass-conservative temporal second order and spatial fourth order characteristic finite volume method (MC-T2S4-CFVM) for solving atmospheric pollution advection diffusion problems is developed. While the characteristics tracking is applied to treat the advection term, we use conservative interpolation to treat the advective integrals over the irregular tracking volume cells at the previous time level. A temporal second order discretization by averaging along the characteristics is proposed for the diffusion term, where the diffusion fluxes are approximated by high order spatial discrete operators that provide continuity of the discrete fluxes across the edges of volume cells and tracking volume cells. The developed characteristic finite volume method is mass conservative and has fourth order accuracy in space and second order accuracy in time. Numerical tests of Gaussian pulse moving verify the temporal and spatial accuracies of MC-T2S4-CFVM as well as the mass-conservative property. The proposed scheme has much better accuracy over the classical characteristic schemes. Computational results of transporting a square of concentration 1 show the high accuracy of MC-T2S4-CFVM in preserving mass and volume. Atmospheric pollution simulations are further carried out by using the MC-T2S4-CFVM. Test results of local emission simulation exhibit the big impact of East Asian monsoon winds on the transport of local emission. The predicted results of $PM_{2.5}$ concentrations in the realistic simulation are consistent with observed data in three metropolitan municipalities and the capitals of seven provinces in China. Investigating through the time series of wind vectors and $PM_{2.5}$ concentration, the influence of wind transport has been numerically observed on the air quality of the cities and provinces. The developed high order mass-conservative characteristic method can be used to solve the large scale atmospheric pollution problems in real-world applications.

Key words. fourth order in space, second order in time, mass conservative, characteristic finite volume method, atmospheric pollution transport

AMS subject classifications. 65M08, 76R99, 86A10

DOI. 10.1137/18M121914X

1. Introduction.

Atmospheric pollution advection diffusion problems refer to the mathematical description and modeling of contaminant transport in the atmosphere. In recent decades, the tremendous increase in emission of air pollutants resulting from rapidly expanding economic and industrial developments has caused serious air pollution, which affects human health and society greatly and is one of the top environmental concerns in many countries. Moreover, suspended pollutant particles can act on climate change directly by altering the scattering properties of the atmosphere, and indirectly by changing cloud properties [31, 50]. Modeling the distribution

*Submitted to the journal's Computational Methods in Science and Engineering section October 5, 2018; accepted for publication (in revised form) July 31, 2019; published electronically November 7, 2019.

https://doi.org/10.1137/18M121914X

Funding: This work was partially supported by the National Natural Science Foundation of China (grant 11601497), the Natural Sciences and Engineering Research Council of Canada, the Fundamental Research Funds for the Central Universities of China (grant 201712003), and the Natural Science Foundation of Shandong Province (grant ZR2016AB16).

†School of Mathematical Sciences, Ocean University of China, Qingdao 266100, People's Republic of China (kfu@ouc.edu.cn).

‡Corresponding author. Department of Mathematics and Statistics, York University, Toronto, ON, M3J 1P3, Canada (dliang@yorku.ca).

and transport of air pollutants can help us to control air pollution effectively, and thus it attracts scientific attention all over the world [22, 50, 51, 52].

The spatial transport of atmospheric contaminant concentrations released into the air can be described by advection diffusion equations, which are advection-dominated diffusion partial differential equations (PDEs) (see [50, 51]). Accurate numerical computation of the problem is a challenging task due to the dominance of the velocity, the large computational region, and the long period prediction. On one hand, for advection-dominated problems where advective stirring sharpens concentration gradients, standard numerical methods such as finite difference methods, finite volume methods, and finite element methods will encounter problems of nonphysical oscillations and excessive numerical dispersions at steep fronts. On the other hand, models of the problems need to be solved over long horizons and over a large number of spatial grid points, so that considerable computational resources are required, especially since the solutions must be obtained over sufficient small time steps to maintain stability and accuracy and to avoid numerical dispersion. Therefore, there is ongoing interest in developing an efficient and highly accurate numerical approach that can solve atmospheric advection diffusion problems simultaneously and can preserve the physical law of mass conservation.

Much effort has been made to solve time-dependent advection diffusion PDEs. One often-used method of simple implementation is implicit-explicit (IMEX) schemes, where the implicit schemes are applied for the diffusion terms, while the explicit schemes are for the advection terms. However, these kinds of schemes have the shortcoming that they are subject to severe CFL restrictions [5, 11], and thus the small time step sizes should be used in computation. Methods of characteristics (MOCs) have been developed for solving advection-dominated PDEs to overcome the CFL condition. MOCs incorporate the fixed Eulerian grids with Lagrangian tracking along the characteristics to treat the advective part of the equations, which allows one to use large time step size. Douglas and Russell first proposed a modified method of characteristics (MMOC) for solving one-dimensional (1D) convection diffusion problems in [18], where a temporal first order characteristics scheme is combined with both finite differences and Lagrange finite elements for time-dependent advection diffusion problems. Lately, developments of the characteristic methods and the characteristics mixed element methods were carried out to solve advection diffusion problems in high dimensions, miscible displacement flows, immiscible displacement flows, and aerosol modeling in [8, 14, 19, 25, 34, 35, 55]. The characteristic methods are efficient as they take advantage of the physical characteristics of the advection diffusion equations. They not only can reduce the nonphysical oscillation and excessive numerical dispersion but also have no stability constraints required on the time step. However, as MOCs do not have the nature of mass conservation, the schemes fail to preserve mass. For advection diffusion problems, Celia et al. [10] proposed an Eulerian-Lagrangian localized adjoint method that conserves mass. Wang et al. [54] developed an Eulerian-Lagrangian localized adjoint method combined with a mixed finite element method solution technique for numerical simulation of coupled systems of compressible miscible displacement flows. Rui and Tabata [48] proposed a conservative characteristic finite element method for the advection diffusion equation. As a proper space-time formulation of the problem, Arbogast and Wheeler [4] developed a characteristics-mixed finite element method preserving mass, for which the important idea was proposed of using the backtracked regions along the characteristics from entire cells. Recently, Arbogast and Huang [3, 2] further developed a modified characteristics-mixed method that conserves both mass and volume of the transported fluid regions, which solved

the problem of inaccurate concentration densities caused by incorrect volumes of characteristic backtracked regions. These conservative methods can preserve mass balance identity well, but are of first order accuracy in time.

Another type of Lagrangian characteristic tracking method is arbitrary Lagrangian-Eulerian (ALE) methods. In ALE methods [17, 26], the nodes of the computational mesh may follow the continuum movement as in the Lagrangian description, or be fixed in an Eulerian manner, or be moved in some arbitrary specified way to provide a continuous rezoning capability. By handling different distortions using different descriptions, the accuracy of numerical solutions can be improved. ALE methods have further been studied and applied by several authors [7, 39, 58, 41]. However, these methods are also of first order accuracy in time step size.

On another aspect, for advection only problems, a number of mass-conserving semi-Lagrangian schemes were developed by conservative remapping/reconstruction techniques, which are mathematically based by applying a mass-preserving parabola or cubic interpolation at previous time levels to achieve local mass conservation. Colella and Woodward [13] proposed a widely used PPM (piecewise parabolic method), which was further discussed for high-dimensional transport problems without diffusion in [42, 61, 59]. WENO (weighted essentially nonoscillatory) reconstruction was developed by Qiu and Christlieb [46] and Qiu and Shu [47] to derive conservative semi-Lagrangian finite difference schemes for advection equations. Huang, Arbogast and Qiu [27] further developed a high order in space Eulerian-Lagrangian WENO finite volume scheme for advection only problems. However, for advection-dominated advection diffusion problems in high dimensions, it is very difficult to achieve high order conservative characteristic schemes that can satisfy mass conservation while maintaining a high order accuracy in both time and space. Therefore, there is great interest and challenge in developing temporal second order and spatial high order characteristic methods for solving advection diffusion equations in atmospheric pollution modeling.

In this paper, a mass-conservative temporal second order and spatial fourth order characteristic finite volume method (MC-T2S4-CFVM) is proposed for solving atmospheric pollution advection diffusion problems. The proposed scheme combines the characteristic method with mass-preserving techniques and provides the advantages of both techniques. It permits the use of large time step sizes to get highly accurate solutions, while achieving mass conservation of pollutants. To get mass-preserving results, while characteristics tracking is applied to treat the advection term, we use conservative interpolation to treat the advective integrals over the irregular tracking volume cells at the previous time level. A temporal second order scheme that averages along the characteristics is proposed for the time discretization of the diffusion term, where the diffusion fluxes are approximated by high order discrete operators that provide continuity of the discrete fluxes across the edges of volume cells and tracking volume cells. The important feature is that the developed characteristic finite volume method is mass conservative and has fourth order accuracy in space and second order accuracy in time for two-dimensional (2D) problems, while permitting the use of large time steps, and is therefore highly suitable for large scale problems. Numerical tests of Gaussian hump moving in solid body rotation and in vortexes demonstrate the temporal and spatial accuracies of MC-T2S4-CFVM as well as its mass conservation property. The computation of transporting a square of concentration in two velocity fields shows clearly that MC-T2S4-CFVM is very capable of conserving mass and volume. The method is also applied to atmospheric local emission simulation and realistic pollution simulation in the north part of China. It is found that the simulation

by MC-T2S4-CFVM generates good predictions when compared with the time series of observed $PM_{2.5}$ concentrations in cities. Result analysis shows that wind direction and speed have strong correlation with the air quality in Qinhuangdao. And strong winds can cause high levels of pollution to travel great distances, such as from Jiangsu to the BTH (Beijing–Tianjin–Hebei) region and the Bohai Sea. The developed high order mass-conservative characteristic finite volume method can be used to solve large scale atmospheric pollution problems in real-world applications.

The paper is structured as follows. Section 2 presents the atmospheric pollution advection diffusion problems. Section 3 proposes the mass-conservative second order in time and fourth order in space characteristic finite volume method. Section 4 explains how to solve the atmospheric pollution system using MC-T2S4-CFVM. Numerical experiments and real-case simulations are shown in section 5. Conclusions are given in section 6.

2. Atmospheric pollution advection diffusion problem. Let $c_l(\vec{x}, t)$ be the mass concentration of pollutant species l ($l = 1, 2, \ldots, s$), and let $\vec{c} = (c_1, c_2, \ldots, c_s)$. The evolutions of c_l, $l = 1, 2, \ldots, s$, are governed by the following equations:

$$\begin{aligned}\frac{\partial c_l}{\partial t} =& -\nabla\cdot(\vec{u}_h c_l) - \frac{\partial(u_\eta c_l)}{\partial \eta}\\ &+\nabla\cdot(K_h\nabla c_l) + \frac{\partial}{\partial\eta}\left(K_\eta\frac{\partial c_l}{\partial\eta}\right) + \mathcal{F}_{l,s}, \qquad l = 1, 2, \ldots, s.\end{aligned} \tag{2.1}$$

The first two terms on the right-hand side of (2.1) represent the horizontal and vertical advections, $\vec{u}_h = (u_x, u_y)$ is the horizontal wind velocity, and u_η is the vertical wind velocity. The second two terms are the diffusion, where $K_h = \mathrm{diag}(K_x, K_y)$ is the horizontal diffusion matrix and K_η is the vertical diffusivity coefficient. $\vec{x} = (x, y, \eta)$ represents the location in space, where x and y are the coordinates in the east-west and south-north directions, and η is the vertical coordinate. The problem is built in a three-dimensional (3D) domain, $[a_x, b_x] \times [a_y, b_y] \times [a_\eta, b_\eta]$, which represents a large region of the atmosphere, where the horizontal dimensions generally range from around a hundred kilometers to several thousand kilometers, while the vertical dimension is only approximately 20 kilometers. Usually, in a real-world simulation, equidistant large mesh sizes are recommended to be used for the horizontal grid, while for the vertical layers, the small vertical step sizes are from 60 meters to 1.5 kilometers along a vertical direction. On the other hand, the effect of horizontal diffusion on the transport of atmospheric pollutants is small with respect to horizontal advection, especially in mesoscale applications, while the effect of vertical diffusion (turbulent mixing) is significant [9, 50]. On the boundary of the domain, the boundary conditions are provided as Neumann or Dirichlet boundary conditions for all pollutant species c_l ($l = 1, 2, \ldots, s$) (see [23]).

$\mathcal{F}_{l,s}$ represents the sources of species including the multicomponent aerosol dynamics on small particle size scale, the chemical reaction, and the direct emission source, given as

$$\mathcal{F}_{l,s} = \mathcal{L}_{l,aero}(\vec{c}) + R_{l,chem}(\vec{c}) + E_{l,emis}, \tag{2.2}$$

where the multicomponent nonlinear aerosol dynamics $\mathcal{L}_{l,aero}(\vec{c})$ describes the condensation, coagulation, and deposition on the small particle size scale [15, 45, 63],

$$\mathcal{L}_{l,aero}(\vec{c}) = \mathcal{L}_{l,cond}(\vec{c}) + \mathcal{L}_{l,coag}(\vec{c}) + \mathcal{L}_{l,dep}(c_l). \tag{2.3}$$

Let v be a particle volume. The condensation term [45, 63] is

$$\mathcal{L}_{l,cond}(\vec{c}) = cH_l(\vec{x}, v, t) - \frac{\partial(c_l v H(\vec{x}, v, t))}{\partial v}, \tag{2.4}$$

with $c = \sum_{l=1}^{s} c_l$, $H_l = (1/v)I_l$, where I_l is the rate of change of the volume of a particle of volume v due to condensation or evaporation of species l, and $\sum_{l=1}^{s} H_l = H$.

The coagulation term is given by [15, 45]

$$\begin{aligned}\mathcal{L}_{l,coag}(\vec{c}) = &\int_{V_{\min}}^{v-V_{\min}} \beta(w, v-w) c_l(\vec{x}, w, t) n(\vec{x}, v-w, t) \mathrm{d}w \\ &-c_l \int_{V_{\min}}^{V_{\max}} \beta(v, w) n(\vec{x}, w, t) \mathrm{d}w,\end{aligned} \tag{2.5}$$

where $n(\vec{x}, v, t)$ is the aerosol number distribution, and $c(\vec{x}, w, t) = \rho v n(\vec{x}, w, t)$, with ρ being the average aerosol density. $\beta(v, w)$ (cm s^{-1}) is the coagulation kernel function.

The deposition term is $\mathcal{L}_{l,dep}(c_l) = v_d c_l$, with

$$v_d = \frac{1}{r_a + r_b + r_a r_b v_{sed}} + v_{sed}, \tag{2.6}$$

where r_a denotes the aerodynamic resistance, r_b denotes the quasi-laminar layer resistance, and v_{sed} is the particle gravitational settling velocity [50].

$R_{l,chem}(\vec{c})$ stands for the nonlinear chemical process that involves multiple chemical species and occurs under certain humidity and temperature conditions. The chemical reaction can be described by the thermodynamics equilibrium model [6, 21, 44]. $E_{l,emis}$, $l = 1, 2, \ldots, s$, represent the direct input rate from emission sources, including vehicle, industry, residential, construction dust, road dust, power generation, agriculture, biomass burning, and others. The emission rates can be provided by emission inventories, such as, for example, the National Emissions Inventory (NEI) [53] and the Multi-resolution Emission Inventory for China (MEIC; see http://meicmodel.org/).

The important development of this paper is that for atmospheric pollutant advection diffusion problems, we develop a high order mass-conservative characteristic method.

3. Conservative characteristic finite volume formulation. Now, we concentrate on solutions of the following advection diffusion problems in a 2D domain:

$$\frac{\partial c}{\partial t} + \nabla \cdot (\vec{u}c) - \nabla \cdot (K \nabla c) = f_s(\mathbf{x}, t), \quad (\mathbf{x}, t) \in \Omega \times (0, T], \tag{3.1}$$

$$(K \nabla c) \cdot \vec{\nu} = 0, \quad (\mathbf{x}, t) \in \Gamma \times (0, T], \tag{3.2}$$

$$c(\mathbf{x}, 0) = c_0(\mathbf{x}), \quad \mathbf{x} \in \Omega, \tag{3.3}$$

where $\mathbf{x} = (x, y)$ is the location in space, $t > 0$ is the time, and $(0, T]$ is the time period; Ω is the 2D domain; $\vec{u} = (u_x(\mathbf{x}, t), u_y(\mathbf{x}, t))$ is the velocity of the field; Γ denotes the boundary of Ω, and $\vec{\nu}$ is the unit outer normal to the boundary Γ; $K = \mathrm{diag}(K_x, K_y)$ is the diffusion tensor with $K_x > 0$ and $K_y > 0$; $f_s(\mathbf{x}, t)$ stands for the given source term; and $c_0(\mathbf{x})$ is the initial concentration.

Let Δt be the time step size, let $N_t = T/\Delta t$ be a total step number, and denote $t^n = n\Delta t$. During each time interval $t \in (t^n, t^{n+1}]$, consider the problem (3.1)–(3.3), with c^n being the value at t^n. Let the characteristic curve be $X(\tau; \mathbf{x}, t^{n+1})$ of (3.1),

for $\tau \in [t^n, t^{n+1})$ along the velocity $\vec{u}$ from any point $(\mathbf{x}, t^{n+1})$, defined by

$$\frac{dX(\tau;\mathbf{x},t^{n+1})}{d\tau} = \vec{u}(X(\tau;\mathbf{x},t^{n+1}),\tau), \quad \tau \in [t^n, t^{n+1}), \tag{3.4}$$

$$X(t^{n+1};\mathbf{x},t^{n+1}) = \mathbf{x}. \tag{3.5}$$

Let $\bar{\mathbf{x}}^n = X(t^n;\mathbf{x},t^{n+1})$ be the intersection of the characteristic line with time level $t = t^n$.

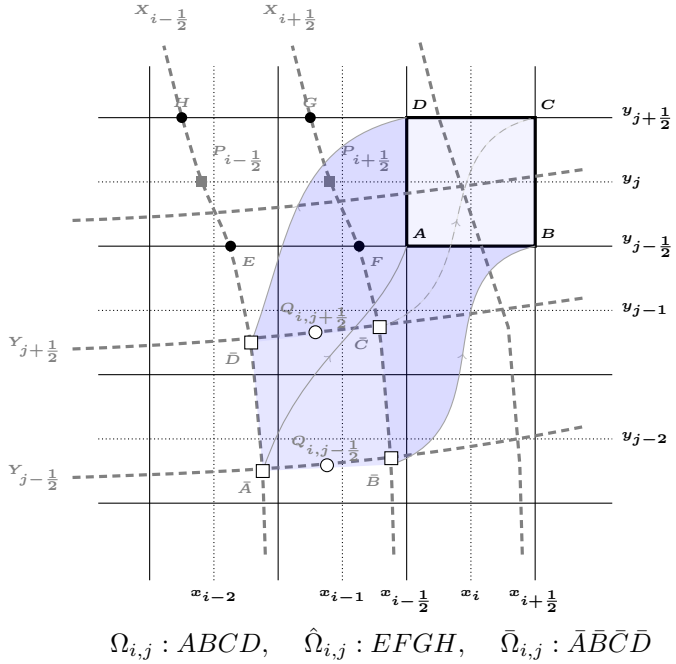

FIG. 1. *Eulerian and Lagrangian mesh grids. Eulerian cells are bounded by continuous thin lines; centered Eulerian lines $x = x_i$ and $y = y_j$ are denoted by thin dotted lines; Lagrangian cells are bounded by thick dashed lines; intersections of Lagrangian lines $X_{i+1/2}$ with centered Eulerian lines $y = y_j$ are denoted by closed gray squares; intersections of Lagrangian lines $X_{i+1/2}$ with Eulerian lines $y = y_{j+1/2}$ are denoted by solid circles; $Q_{i+1/2}$ and $Q_{i-1/2}$ are centers of $\widehat{\bar{A}\bar{B}}$ and $\widehat{\bar{C}\bar{D}}$, respectively.*

Now consider the spatial discretization. Let $\Omega = [x_{\min}, x_{\max}] \times [y_{\min}, y_{\max}]$ be divided into $I_x \times I_y$ regular Eulerian cells $\Omega_{i,j}$, defined as

$$\Omega_{i,j} = \{(x,y), x \in [x_{i-1/2}, x_{i+1/2}], y \in [y_{j-1/2}, y_{j+1/2}]\}, \quad i = 1,2,\ldots,I_x, j = 1,2,\ldots,I_y, \tag{3.6}$$

where $x_{i-1/2} = x_{\min} + (i-1)h_x$, $y_{j-1/2} = y_{\min} + (j-1)h_y$, $h_x = (x_{\max} - x_{\min})/I_x$, and $h_y = (y_{\max} - y_{\min})/I_y$. Thus, the mesh is defined as

$$\Omega_h = \{\Omega_{i,j}, 1 \le i \le I_x, 1 \le j \le I_y\}. \tag{3.7}$$

For each $\Omega_{i,j}$, let $\Omega_{i,j}(t)$ be the corresponding characteristic tracking region at t,

$$\Omega_{i,j}(t) = \{\bar{\mathbf{x}} \in \Omega : \bar{\mathbf{x}} = X(t;\mathbf{x},t^{n+1}), \mathbf{x} \in \Omega_{i,j}\} \text{ for } t \in [t^n, t^{n+1}), \tag{3.8}$$

and let the backtracked region at t^n be

$$\bar{\Omega}_{i,j}(t^n) = \{\bar{\mathbf{x}} \in \Omega : \bar{\mathbf{x}} = X(t^n; \mathbf{x}, t^{n+1}), \mathbf{x} \in \Omega_{i,j}\}. \tag{3.9}$$

Referring to Figure 1, let (X, Y) denote the Lagrangian coordinate system corresponding with the Eulerian (x, y) coordinate system. Define the Lagrangian curve associated with Eulerian line $x = x_{i+1/}$ by $X_{i+1/2}$, and Lagrangian curve associated with Eulerian line $y = y_{i+1/}$ by $Y_{i+1/2}$. Then we get Lagrangian cells with curvilinear boundaries. In Figure 1, the curved quadrilateral $\bar{A}\bar{B}\bar{C}\bar{D}$ is the Lagrangian cell $\bar{\Omega}_{i,j}$ associated with Eulerian cell $\Omega_{i,j} : ABCD$. Let $\hat{\Omega}_{i,j}$ $(EFGH)$ be the volume bounded in the x-direction by $y = y_{i-\frac{1}{2}}$ and $y = y_{i+\frac{1}{2}}$, and bounded within the Lagrangian lines of $X_{i-\frac{1}{2}}$ and $X_{i+\frac{1}{2}}$.

Integrating the governing equation (3.1) in space and time over $\{(\mathbf{x}, t); \mathbf{x} \in \Omega_{i,j}(t), t \in [t^n, t^{n+1}]\}$ leads to

$$\int_{t^n}^{t^{n+1}} \int_{\Omega_{i,j}(t)} \left(\frac{\partial c}{\partial t} + \nabla \cdot (\vec{u}c)\right) \mathrm{d}\mathbf{x}\mathrm{d}t - \int_{t^n}^{t^{n+1}} \int_{\Omega_{i,j}(t)} \nabla \cdot (K \nabla c) \mathrm{d}\mathbf{x}\mathrm{d}t = \int_{t^n}^{t^{n+1}} \int_{\Omega_{i,j}(t)} f_s(\mathbf{x}, t) \mathrm{d}\mathbf{x}\mathrm{d}t. \tag{3.10}$$

By applying the Leibniz rule for the differentiation of an integral in the plane [20], we have

$$\frac{\mathrm{d}}{\mathrm{d}t}\left(\int_{\Omega_{i,j}(t)} c(\mathbf{x}, t) \mathrm{d}\mathbf{x}\right) = \int_{\Omega_{i,j}(t)} \left(\frac{\partial c}{\partial t} + \nabla \cdot (\vec{u}c)\right) \mathrm{d}\mathbf{x}, \tag{3.11}$$

and substituting (3.11) into the first term of (3.10) yields

$$\int_{t^n}^{t^{n+1}} \int_{\Omega_{i,j}(t)} \left(\frac{\partial c}{\partial t} + \nabla \cdot (\vec{u}c)\right) \mathrm{d}\mathbf{x}\mathrm{d}t = \int_{\Omega_{i,j}} c(\mathbf{x}, t^{n+1}) \mathrm{d}\mathbf{x} - \int_{\bar{\Omega}_{i,j}(t^n)} c(\mathbf{x}, t^n) \mathrm{d}\mathbf{x}. \tag{3.12}$$

For the diffusion term of (3.10), noting the definition of $\Omega_{i,j}(t)$ in (3.8), the following temporal second order approximation along the characteristics is proposed:

$$\begin{aligned} &\int_{t^n}^{t^{n+1}} \int_{\Omega_{i,j}(t)} \nabla \cdot (K \nabla c) \mathrm{d}\mathbf{x}\mathrm{d}t = \int_{t^n}^{t^{n+1}} \int_{\partial\Omega_{i,j}(t)} (K \nabla c) \cdot \vec{\nu} \mathrm{d}\mathbf{x}\mathrm{d}t \\ &= \frac{\Delta t}{2}\left(\int_{\partial\Omega_{i,j}} (K \nabla c(\mathbf{x}, t^{n+1})) \cdot \vec{\nu} \mathrm{d}\mathbf{x} + \int_{\partial\bar{\Omega}_{i,j}(t^n)} (K \nabla c(\mathbf{x}, t^n)) \cdot \vec{\nu} \mathrm{d}\mathbf{x}\right) + O(\Delta t^3), \end{aligned} \tag{3.13}$$

where $\partial\Omega_{i,j}$ and $\partial\Omega_{i,j}(t)$ are the boundaries of $\Omega_{i,j}$ and $\Omega_{i,j}(t)$, and $\vec{\nu}$ is the unit outer normal to the boundaries. Then a semidiscrete mass-conservative equation for the 2D advection diffusion problem (3.1) is proposed as

$$\begin{aligned} &\int_{\Omega_{i,j}} c(\mathbf{x}, t^{n+1}) \mathrm{d}\mathbf{x} - \int_{\bar{\Omega}_{i,j}(t^n)} c(\mathbf{x}, t^n) \mathrm{d}\mathbf{x} \\ &\quad - \frac{\Delta t}{2}\left(\int_{\partial\Omega_{i,j}} (K \nabla c(\mathbf{x}, t^{n+1})) \cdot \vec{\nu} \mathrm{d}\mathbf{x} + \int_{\partial\bar{\Omega}_{i,j}(t^n)} (K \nabla c(\mathbf{x}, t^n)) \cdot \vec{\nu} \mathrm{d}\mathbf{x}\right) \\ &\quad = \int_{t^n}^{t^{n+1}} \int_{\Omega_{i,j}(t)} f_s(\mathbf{x}, t) \mathrm{d}\mathbf{x}\mathrm{d}t. \end{aligned} \tag{3.14}$$

Let $C_{i,j}$ be the approximation to the cell-averaged concentration $c(\mathbf{x},t)$ at time t on cell $\Omega_{i,j}$. Then

$$\int_{\Omega_{i,j}} c(\mathbf{x},t^{n+1})\mathrm{d}\mathbf{x} \approx h_x h_y C_{i,j}^{n+1}. \tag{3.15}$$

In order to get mass conservation and high order accuracy, we approximate the second term of $\int_{\bar{\Omega}_{i,j}(t^n)} c(\mathbf{x},t^n)\mathrm{d}\mathbf{x}$ on the tracking volume region $\bar{\Omega}_{i,j}(t^n)$ by using a particular interpolation of the PPM (piecewise parabolic method) in [13, 43]. The approximation is defined in the following two stages.

Stage 1. Perform a high order conservative computation over a single y_j strip, $j = 1,\ldots,I_y$. Let's consider the subdomain within the lines $y_{j-\frac{1}{2}}$ and $y_{j+\frac{1}{2}}$, and define a mass-preserving interpolation distribution $[\mathcal{R}^x C^n]_{p,j}$, $p = 1,\ldots,I_x$,

$$[\mathcal{R}^x C^n]_{p,j}(x) = \langle C^n\rangle_{p-\frac{1}{2},j} + \frac{x - x_{p-\frac{1}{2}}}{h_x}\left(\Delta C_{p,j}^n + C_{6,p,j}^n \frac{x_{p+\frac{1}{2}} - x}{h_x}\right), \tag{3.16}$$

which satisfies

$$\begin{cases} [\mathcal{R}^x C^n]_{p,j}(x_{p-\frac{1}{2}}) = \langle C^n\rangle_{p-\frac{1}{2},j}, \\ [\mathcal{R}^x C^n]_{p,j}(x_{p+\frac{1}{2}}) = \langle C^n\rangle_{p+\frac{1}{2},j}, \\ \int_{x_{p-\frac{1}{2}}}^{x_{p+\frac{1}{2}}} [\mathcal{R}^x C^n]_{p,j}(x)\mathrm{d}x = h_x C_{p,j}^n, \end{cases} \tag{3.17}$$

where, for fixed j, $\Delta C_{p,j}^n$, $C_{6,p,j}^n$, $\langle C^n\rangle_{p-\frac{1}{2},j}$ are computed for fourth order accuracy in space as below:

$$\langle C^n\rangle_{p+\frac{1}{2},j} = \frac{7}{12}(C_{p,j}^n + C_{p+1,j}^n) - \frac{1}{12}(C_{p+2,j}^n + C_{p-1,j}^n), \tag{3.18}$$

$$\Delta C_{p,j}^n = \langle C^n\rangle_{p+\frac{1}{2},j} - \langle C^n\rangle_{p-\frac{1}{2},j}, \tag{3.19}$$

$$C_{6,p,j}^n = 6\left(C_{p,j}^n - \frac{1}{2}(\langle C^n\rangle_{p+\frac{1}{2},j} + \langle C^n\rangle_{p-\frac{1}{2},j})\right). \tag{3.20}$$

$[\mathcal{R}^x C^n]_{p,j}$ defines a mass-conservative distribution along an Eulerian x-direction over $\Omega_{p,j}$.

When $p = 0, 1, I_x - 1$, and I_x, "ghost cells" are used to evaluate the value of $\langle C^n\rangle_{p+\frac{1}{2},j}$. Let $C_{-1,j}$, $C_{0,j}$, $C_{I_x+1,j}$, and $C_{I_x+2,j}$ denote the averaged concentrations on "ghost cells" $\Omega_{-1,j}$, $\Omega_{0,j}$, $\Omega_{I_x+1,j}$, and $\Omega_{I_x+2,j}$. In the case of the given Neumann boundary condition (3.2), that is, $\frac{\partial c}{\partial x} = 0$ at $x = x_{\frac{1}{2}}$ and $x = x_{I_x+\frac{1}{2}}$, we have the fourth order formulas of "ghost cell" values

$$C_{0,j} = \frac{1}{11}\left(-C_{3,j} + 3C_{2,j} + 9C_{1,j}\right), \tag{3.21}$$

$$C_{-1,j} = \frac{1}{11}\left(-15C_{3,j} + 56C_{2,j} - 30C_{1,j}\right), \tag{3.22}$$

$$C_{I_x+1,j} = \frac{1}{11}\left(-C_{I_x-2,j} + 3C_{I_x-1,j} + 9C_{I_x,j}\right), \tag{3.23}$$

$$C_{I_x+2,j} = \frac{1}{11}\left(-15C_{I_x-2,j} + 56C_{I_x-1,j} - 30C_{I_x,j}\right). \tag{3.24}$$

Let $P_{i+\frac{1}{2},j}(\tilde{x}_{i+\frac{1}{2},j}, y_j)$ be the intersection point of $X_{i+\frac{1}{2}}$ with the line $y = y_j$.

Then, on the intermediate cell $\hat{\Omega}_{i,j}$, we have the mass

$$\int_{\hat{\Omega}_{i,j}} c^n(\mathbf{x})\mathrm{d}\mathbf{x} \approx h_y \int_{\tilde{x}_{i-1/2,j}}^{\tilde{x}_{i+1/2,j}} [\mathcal{R}^x C^n](x,t^n)\mathrm{d}x \tag{3.25}$$
$$= \begin{cases} h_y \int_{\tilde{x}_{i-1/2,j}}^{x_{l+\frac{1}{2}}} [\mathcal{R}^x C^n]_{l,j}(x)\mathrm{d}x + \sum_{p=l+1}^{m-1} h_y h_x C^n_{p,j} \\ \qquad + h_y \int_{x_{m-\frac{1}{2}}}^{\tilde{x}_{i+1/2}} [\mathcal{R}^x C^n]_{m,j}(x)\mathrm{d}x, & m \geq l+1, \\ h_y \int_{\tilde{x}_{i-1/2,j}}^{\tilde{x}_{i+1/2,j}} [\mathcal{R}^x C^n]_{l,j}(x)\mathrm{d}x, & m = l, \end{cases}$$

where m and l ($m \geq l$) are the x-indices of Eulerian cells within which $\tilde{x}_{i+1/2,j}$ and $\tilde{x}_{i-1/2,j}$ lie.

Stage 2. Perform a high order conservative computation over the X_i Lagrangian strip, $i = 1, 2, \ldots, I_x$. Consider the subdomain within Lagrangian lines $X_{i-\frac{1}{2}}$ and $X_{i+\frac{1}{2}}$, which is denoted by the X_i Lagrangian strip. Given the mass over each $\hat{\Omega}_{i,q}$ computed in Stage 1, let $\hat{C}^n_{i,q} = \int_{\tilde{x}_{i-1/2,j}}^{\tilde{x}_{i+1/2,j}} [\mathcal{R}^x C^n]\ (x,t^n)\mathrm{d}x$. For a fixed i, we define a high order mass-conservative interpolation function $[\mathcal{R}^y \hat{C}^n]_{i,q}$, $q = 1, 2, \ldots, I_y$:

$$[\mathcal{R}^y \hat{C}^n]_{i,q}(y) = \langle \hat{C}^n \rangle_{i-\frac{1}{2},q} + \frac{y - y_{q-\frac{1}{2}}}{h_y} \left(\Delta \hat{C}^n_{i,q} + \hat{C}^n_{6,i,q} \frac{y_{q+\frac{1}{2}} - y}{h_y} \right), \tag{3.26}$$

which satisfies

$$\begin{cases} [\mathcal{R}^y \hat{C}^n]_{i,q}(y_{q-\frac{1}{2}}) = \langle \hat{C}^n \rangle_{i,q-\frac{1}{2}}, \\ [\mathcal{R}^y \hat{C}^n]_{i,q}(y_{q+\frac{1}{2}}) = \langle \hat{C}^n \rangle_{i,q+\frac{1}{2}}, \\ \int_{y_{q-\frac{1}{2}}}^{y_{q+\frac{1}{2}}} [\mathcal{R}^y \hat{C}^n]_{i,q}(y)\mathrm{d}y = h_y \hat{C}^n_{i,q}, \end{cases} \tag{3.27}$$

where $\langle \hat{C}^n \rangle_{i-\frac{1}{2},q}$ is computed by using the fourth order approximation (3.18), and $\Delta \hat{C}^n_{i,q}$, $\hat{C}^n_{6,i,q}$ are computed by using (3.19) and (3.20), respectively. When $q = 0, 1, I_y - 1$, and I_y, $\langle \hat{C}^n \rangle_{i-\frac{1}{2},q}$ can be computed by "ghost cells," similarly as in (3.21)–(3.24) in Stage 1. Here, $[\mathcal{R}^y \hat{C}^n]_{i,q}$ provides a high order conservative concentration distribution on cell $\hat{\Omega}_{i,q}$ along the y-direction. Let $Q_{i,j+\frac{1}{2}}$ $(\tilde{x}_{i,j+\frac{1}{2}}, \tilde{y}_{i,j+\frac{1}{2}})$ be the middle point of $\bar{\mathbf{x}}_{i-\frac{1}{2},j+\frac{1}{2}}$ and $\bar{\mathbf{x}}_{i+\frac{1}{2},j+\frac{1}{2}}$. The mass over the Lagrangian tracking cell $\bar{\Omega}_{i,j}$ at the t^n level is then approximated by an integral from the point $Q_{i,j-\frac{1}{2}}$ to $Q_{i,j+\frac{1}{2}}$,

$$\int_{\bar{\Omega}_{i,j}} c^n(\mathbf{x},t)\mathrm{d}\mathbf{x} \approx \int_{\tilde{y}_{i,j-1/2}}^{\tilde{y}_{i,j+1/2}} [\mathcal{R}^y \hat{C}^n](y,t^n)\mathrm{d}y \tag{3.28}$$
$$= \begin{cases} \int_{\tilde{y}_{i,j-1/2}}^{y_{l_y+\frac{1}{2}}} [\mathcal{R}^y \hat{C}^n]_{i,l_y}(y)\mathrm{d}y + \sum_{q=l_y+1}^{m_y-1} h_y \hat{C}^n_{i,q} \\ \qquad + \int_{y_{m_y-\frac{1}{2}}}^{\tilde{y}_{i,j+1/2}} [\mathcal{R}^y \hat{C}^n]_{i,m_y}(y)\mathrm{d}y, & m_y \geq l_y + 1, \\ \int_{\tilde{y}_{i,j-1/2}}^{\tilde{y}_{i,j+1/2}} [\mathcal{R}^y \hat{C}^n]_{i,l_y}(y)\mathrm{d}y, & m_y = l_y, \end{cases}$$
$$\equiv I_{h,\bar{\Omega}_{i,j}}(C^n),$$

where l_y and m_y ($m_y \geq l_y$) are the y-indices of $\hat{\Omega}_{i,q}$ within which $\tilde{y}_{i,j-1/2}$ and $\tilde{y}_{i,j+1/2}$ lie.

To the third term of (3.14), the diffusion term with variable coefficient at time level t^{n+1}, we have the following conservative fourth order approximation [29]:

$$\begin{aligned}(3.29)\qquad &\frac{1}{h_x h_y}\int_{\partial\Omega_{i,j}}(K\nabla c(\mathbf{x},t^{n+1}))\cdot\vec{\nu}\mathrm{d}\mathbf{x}\\ &=\frac{1}{h_x}\left(H_{i+\frac{1}{2},j}(c^{n+1})-H_{i-\frac{1}{2},j}(c^{n+1})\right)\\ &\quad+\frac{1}{h_y}\left(H_{i,j+\frac{1}{2}}(c^{n+1})-H_{i,j-\frac{1}{2}}(c^{n+1})\right)+O(h_x^4)+O(h_y^4),\end{aligned}$$

with $H(c)$ being the continuous flux defined by

$$(3.30)\qquad H_{i+\frac{1}{2},j}(c)=\frac{1}{h_x}\sum_{l=-1}^{2}\sum_{m=-1}^{2}M_{l,m}K_{x_{i+l,j}}c_{i+m,j},$$

$$(3.31)\qquad H_{i,j+\frac{1}{2}}(c)=\frac{1}{h_y}\sum_{l=-1}^{2}\sum_{m=-1}^{2}M_{l,m}K_{y_{i,j+l}}c_{i,j+m},$$

where $M=\{M_{m,n}\}$ is given by

$$(3.32)\qquad M=\begin{bmatrix}\frac{1}{8}&-\frac{1}{6}&\frac{1}{24}&0\\ -\frac{1}{6}&-\frac{3}{8}&\frac{2}{3}&\frac{1}{8}\\ \frac{1}{8}&-\frac{2}{3}&\frac{3}{8}&\frac{1}{6}\\ 0&-\frac{1}{24}&\frac{1}{6}&-\frac{1}{8}\end{bmatrix}.$$

The computation of the diffusion term at time level t^n, i.e., $\int_{\partial\bar{\Omega}_{i,j}(t^n)}(K\nabla c(\mathbf{x},t^n))\cdot\vec{\nu}\mathrm{d}\mathbf{s}$, is difficult since the tracked region boundaries are not aligned with the regular Eulerian mesh. In order to get accurate approximation and preserve mass, we require that the discrete flux at t^n remains continuous at tracked region boundaries and has high order accuracy. Thus we propose to approximate the scalar field of c^n by a piecewise biquartic function, from which we get the diffusion flux that is continuous at the tracked region boundaries at time level t^n. Based on the average values $C_{i,j}$, we define the piecewise biquartic function on $\Omega_{i,j}$ as

$$\begin{aligned}(3.33)\qquad [\mathcal{B}C^n]_{i,j}(x,y)&=\sum_{k,l=-2}^{2}N_k(\xi)N_l(\eta)C_{i+k,j+l},\\ &\quad\forall n\geq 0,\ i=1,2,\ldots,I_x,j=1,2,\ldots,I_y,\end{aligned}$$

where

$$(3.34)\qquad \xi=(x-x_i)/\Delta x,\ \eta=(y-y_j)/\Delta y,$$

$$(3.35)\qquad \begin{cases}N_{-2}(\xi)=\frac{1}{24}(\xi+1)\xi(\xi-1)(\xi-2),\\ N_{-1}(\xi)=-\frac{1}{6}(\xi+2)\xi(\xi-1)(\xi-2),\\ N_0(\xi)=\frac{1}{4}(\xi+2)(\xi+1)(\xi-1)(\xi-2),\\ N_1(\xi)=-\frac{1}{6}(\xi+2)(\xi+1)\xi(\xi-2),\\ N_{-2}(\xi)=\frac{1}{24}(\xi+2)(\xi+1)\xi(\xi-1).\end{cases}$$

Assume that one boundary of the tracked region $\bar{\Omega}_{i,j}$ is divided into several small parts $\{e_s\}$ by intersections of the boundary with the Eulerian grid lines. We take

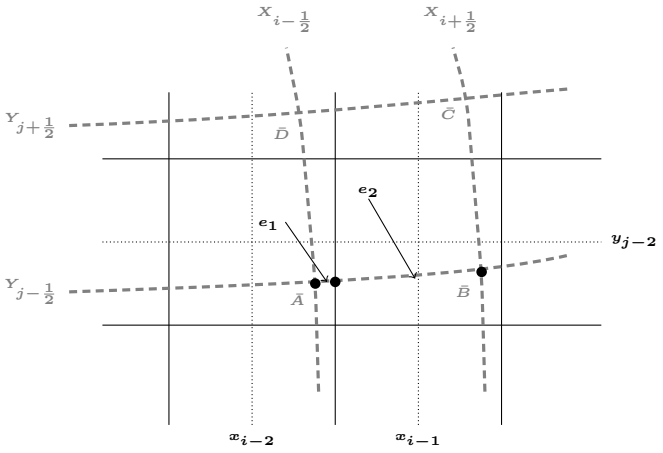

FIG. 2. *The mesh around the tracking characteristic cell.*

$\int_{\widehat{\bar{A}\bar{B}}}(K\nabla c^n)\cdot\vec{\nu}ds$ (Figure 2) as an example. The integral over $\widehat{\bar{A}\bar{B}}$ can be understood as a sum of the elementary integrals over these small parts of e_1 and e_2 in different grid cells of $\Omega_{i-2,j-2}$ and $\Omega_{i-1,j-2}$ (Figure 2):

$$\int_{\widehat{\bar{A}\bar{B}}}(K\nabla c^n)\cdot\vec{\nu}ds=\sum_{e_s}I_s=I_1+I_2. \tag{3.36}$$

Here I_s is an elementary integral over the small parts e_s. Since we already have the piecewise function $[\mathcal{B}C^n]$ on each $\Omega_{i,j}$, the integral can be obtained by

$$\begin{aligned}\int_{\widehat{\bar{A}\bar{B}}}(K\nabla c^n)\cdot\vec{\nu}ds&\approx\sum_s\int_{e_s}(K\nabla[\mathcal{B}C^n])\cdot\vec{\nu}ds\\&=\int_{e_1}(K\nabla[\mathcal{B}C^n]_{i-2,j-2})\cdot\vec{\nu}ds+\int_{e_2}(K\nabla[\mathcal{B}C^n]_{i-1,j-2})\cdot\vec{\nu}ds\\&\equiv DI_{h,\partial\bar{\Omega}_{i,j,S}}.\end{aligned} \tag{3.37}$$

Approximations of integrals $\int_{\widehat{\bar{B}\bar{C}}}$, $\int_{\widehat{\bar{C}\bar{D}}}$, and $\int_{\widehat{\bar{D}\bar{A}}}$ can be similarly obtained, and we denote them as $DI_{h,\partial\bar{\Omega}_{i,j,E}}(C^n)$, $DI_{h,\partial\bar{\Omega}_{i,j,N}}(C^n)$, and $DI_{h,\partial\bar{\Omega}_{i,j,W}}(C^n)$, where the letters S,E,N,W represent the "south," "east," "north," and "west" boundaries of $\partial\bar{\Omega}_{i,j}$, respectively. Then we have

$$\begin{aligned}&\int_{\partial\bar{\Omega}_{i,j}(t^n)}(K\nabla c(\mathbf{x},t^n))\cdot\vec{\nu}\mathrm{d}\mathbf{x}\\&=DI_{h,\partial\bar{\Omega}_{i,j,E}}(C^n)+DI_{h,\partial\bar{\Omega}_{i,j,W}}(C^n)+DI_{h,\partial\bar{\Omega}_{i,j,N}}(C^n)+DI_{h,\partial\bar{\Omega}_{i,j,S}}(C^n).\end{aligned} \tag{3.38}$$

From (3.14) to (3.38), the mass-conservative temporal second order and spatial fourth order characteristic finite volume method (MC-T2S4-CFVM) for solving the

2D advection diffusion problem (3.1) is proposed as

$$\begin{aligned}
&\Big(h_x h_y C_{i,j}^{n+1} - I_{h,\bar{\Omega}_{i,j}}(C^n)\Big) \\
&-\frac{\Delta t}{2}\Big[\Big(h_y(H_{i+\frac{1}{2},j}(C^{n+1}) - H_{i-\frac{1}{2},j}(C^{n+1})) \\
&\qquad +h_x(H_{i,j+\frac{1}{2}}(C^{n+1}) - H_{i,j-\frac{1}{2}}(C^{n+1}))\Big) \qquad (3.39)\\
&\qquad +\Big(DI_{h,\partial\bar{\Omega}_{i,j,E}}(C^n) + DI_{h,\partial\bar{\Omega}_{i,j,W}}(C^n) \\
&\qquad +DI_{h,\partial\bar{\Omega}_{i,j,N}}(C^n) + DI_{h,\partial\bar{\Omega}_{i,j,S}}(C^n)\Big)\Big] \qquad (3.40)\\
&= \int_{t^n}^{t^{n+1}} \int_{\Omega_{i,j}(t)} f_s(x,t)\mathrm{d}\mathbf{x}\mathrm{d}t,
\end{aligned}$$

the initial condition is $C^0(x_i, y_j) = c_{i,j}^0$, and the boundary conditions are set as

$$\begin{aligned}
&H_{\frac{1}{2},j}(C^{n+1}) = 0,\ H_{I_x+\frac{1}{2},j}(C^{n+1}) = 0, \quad j = 1, 2, \ldots, I_y,\ n = 1, 2, \ldots, N_t, \\
&H_{i,\frac{1}{2}}(C^{n+1}) = 0,\ H_{i,,I_y+\frac{1}{2}}(C^{n+1}) = 0, \quad i = 1, 2, \ldots, I_x,\ n = 1, 2, \ldots, N_t.
\end{aligned} \qquad (3.41)$$

On the domain boundary, $\vec{u}\cdot\vec{\nu} = 0$ on $\partial\Omega$ represents a no-flow condition, while $\vec{u}\cdot\vec{\nu} < 0$ on $\partial\Omega$ and $\vec{u}\cdot\vec{\nu} > 0$ on $\partial\Omega$ represent inflow and outflow conditions, respectively. We now examine the mass-preserving property of the proposed MC-T2S4-CFVM (3.39), where the velocity field $\vec{u}$ satisfies the following condition.

Hypothesis 3.1. The velocity $\vec{u} \in C^0(W^{1,\infty}(\Omega))$ satisfies

$$\vec{u}\cdot\vec{\nu} = 0 \ \text{ on } \partial\Omega. \qquad (3.42)$$

THEOREM 3.2. *Under Hypothesis* 3.1*, consider problem* (3.1) *with Neumann boundary condition*

$$(K\nabla c)\cdot\vec{\nu} = 0 \quad \textit{on } \partial\Omega. \qquad (3.43)$$

Scheme (3.39) *is globally mass conservative.*

Proof. Summing (3.39) from $i = 1$ to I_x, and $j = 1$ to I_y leads to

$$\begin{aligned}
&\sum_{i=1}^{I_x}\sum_{j=1}^{I_y} h_x h_y C_{i,j}^{n+1} - \sum_{i=1}^{I_x}\sum_{j=1}^{I_y} I_{h,\bar{\Omega}_{i,j}}(C^n) \\
&-\frac{\Delta t}{2}\sum_{i=1}^{I_x}\sum_{j=1}^{I_y}\Big(h_y(H_{i+\frac{1}{2},j}(C^{n+1}) - H_{i-\frac{1}{2},j}(C^{n+1})) \\
&\qquad +h_x(H_{i,j+\frac{1}{2}}(C^{n+1}) - H_{i,j-\frac{1}{2}}(C^{n+1}))\Big) \\
&-\frac{\Delta t}{2}\sum_{i=1}^{I_x}\sum_{j=1}^{I_y}\Big(DI_{h,\partial\bar{\Omega}_{i,j,R}}(C^n) + DI_{h,\partial\bar{\Omega}_{i,j,L}}(C^n) \\
&\qquad +DI_{h,\partial\bar{\Omega}_{i,j,T}}(C^n) + DI_{h,\partial\bar{\Omega}_{i,j,B}}(C^n)\Big) \qquad (3.44)\\
&= \int_{t^n}^{t^{n+1}} \int_{\Omega} f_s(\mathbf{x},t) d\mathbf{x} dt.
\end{aligned}$$

Under Hypothesis 3.1, for any $j = 0, 1, \ldots, I_y$, we have $\bar{x}_{\frac{1}{2},j} = x_{\frac{1}{2},j} = x_{\min}$, $\bar{x}_{I_x+\frac{1}{2},j} = x_{I_x+\frac{1}{2},j} = x_{\max}$, and for any $i = 0, 1, \ldots, I_x$, we have $\bar{y}_{i,\frac{1}{2}} = y_{j,\frac{1}{2}} = y_{\min}$, $\bar{y}_{i,I_y+\frac{1}{2}} = y_{i,I_y+\frac{1}{2}} = y_{\max}$. Noting that approximated characteristic curves do not cross each other, and combined with (3.26), this leads to

$$\sum_{i=1}^{I_x} \hat{M}_{i,j}^n = \sum_{i=1}^{I_x} I_{h,\hat{\Omega}_{i,j}}(C^n) = \sum_{i=1}^{I_x} h_y h_x C_{i,j}^n, \tag{3.45}$$

where $\hat{M}_{i,j}^n$ is the mass over the intermediate cell $\hat{\Omega}_{i,j}$ computed by (3.26). Combined with (3.28), this gives

$$\sum_{j=1}^{I_y} I_{h,\bar{\Omega}_{i,j}}(C^n) = \sum_{j=1}^{I_y} I_{h,\hat{\Omega}_{i,j}}(C^n) = \sum_{j=1}^{I_y} \hat{M}_{i,j}^n, \tag{3.46}$$

which yields

$$\sum_{i=1}^{I_x}\sum_{j=1}^{I_y} I_{h,\bar{\Omega}_{i,j}}(C^n) = \sum_{j=1}^{I_y}\sum_{i=1}^{I_x} h_x h_y C_{i,j}^n. \tag{3.47}$$

According to the given Neumann boundary condition (3.2) and (3.41), and the continuity of $H_{i+\frac{1}{2},j}(C^{n+1})$ and $H_{i,j+\frac{1}{2}}(C^{n+1})$, it is easy to see that

$$\begin{aligned}
&\sum_{i=1}^{I_x}\sum_{j=1}^{I_y} \Big(h_y(H_{i+\frac{1}{2},j}(C^{n+1}) - H_{i-\frac{1}{2},j}(C^{n+1})) \\
&\qquad + h_x(H_{i,j+\frac{1}{2}}(C^{n+1}) - H_{i,j-\frac{1}{2}}(C^{n+1}))\Big) \\
&= \sum_{i=1}^{I_x} \Big(h_x(H_{i,I_y+\frac{1}{2}}(C^{n+1}) - H_{i,\frac{1}{2}}(C^{n+1}))\Big) \\
&\quad + \sum_{j=1}^{I_y} \Big(h_y(H_{I_x+\frac{1}{2},j}(C^{n+1}) - H_{\frac{1}{2},j}(C^{n+1}))\Big) = 0.
\end{aligned} \tag{3.48}$$

For the diffusion term at t^n, as the approximated characteristic curves do not cross each other, and under Hypothesis 3.1, the entire tracking domain is exactly the same as the computed Eulerian domain Ω. Noting that for two adjacent Lagrangian cells which share one boundary, such as $\bar{\Omega}_{i,j}$ and $\bar{\Omega}_{i,j-1}$ share the boundary $\widehat{\bar{A}\bar{B}}$ (Figure 1), $\widehat{\bar{A}\bar{B}}$ is the "south" boundary of $\bar{\Omega}_{i,j}$ and "north" boundary of $\bar{\Omega}_{i,j-1}$ at the same time. The discrete fluxes across the "south" boundary of $\bar{\Omega}_{i,j}$ (denoted by $DI_{h,\partial\bar{\Omega}_{i,j,S}}$) and the "north" boundary of $\bar{\Omega}_{i,j-1}$ (denoted by $DI_{h,\partial\bar{\Omega}_{i,j-1,N}}$) are both given by summation of the approximated flux over divided small parts in Eulerian grid cells (3.37). As in each Eulerian grid cell, the piecewise biquartic function $[\mathcal{B}C^n]$ (3.33) is a fixed function, such that the discrete fluxes for $\bar{\Omega}_{i,j}$ and $\bar{\Omega}_{i,j-1}$ over each small part of $\widehat{\bar{A}\bar{B}}$ have exactly the same value with opposite sign. Hence the fluxes $DI_{h,\partial\bar{\Omega}_{i,j,S}}$ and $DI_{h,\partial\bar{\Omega}_{i,j-1,N}}$ also have exactly the same value with opposite sign, i.e.,

$$DI_{h,\partial\bar{\Omega}_{i,j,S}}(C^n) + DI_{h,\partial\bar{\Omega}_{i,j-1,N}}(C^n) = 0. \tag{3.49}$$

Similarly, we have

$$DI_{h,\partial\bar{\Omega}_{i,j,W}}(C^n) + I_{h,\partial\bar{\Omega}_{i-1,j,E}}(C^n) = 0. \tag{3.50}$$

Considering the boundary condition (3.43), the corresponding fluxes over the domain boundary sum up to zero; hence the sum of discrete fluxes over the whole computational domain vanishes,

$$\begin{aligned}\sum_{i=1}^{I_x}\sum_{j=1}^{I_y}\Big(&DI_{h,\partial\bar{\Omega}_{i,j,E}}(C^n) + DI_{h,\partial\bar{\Omega}_{i,j,W}}(C^n)\\ &+DI_{h,\partial\bar{\Omega}_{i,j,N}}(C^n) + DI_{h,\partial\bar{\Omega}_{i,j,S}}(C^n)\Big) = 0.\end{aligned} \tag{3.51}$$

Then from (3.44)–(3.51), it holds that

$$\sum_{i=1}^{I_x}\sum_{j=1}^{I_y} h_x h_y C_{i,j}^{n+1} - \sum_{i=1}^{I_x}\sum_{j=1}^{I_y} h_x h_y C_{i,j}^{n} = \int_{t^n}^{t^{n+1}}\int_{\Omega} f_s(\mathbf{x},t)d\mathbf{x}dt. \tag{3.52}$$

This ends the proof. ∎

Remark 3.3. In implementation, the second order Runge–Kutta method can be used to solve (3.4) and (3.5) for the approximate characteristics as

$$\bar{\mathbf{x}}^n = \mathbf{x} - \frac{1}{2}\left[u(\mathbf{x},t^{n+1}) + u(\mathbf{x}-u(\mathbf{x},t^{n+1})\Delta t, t^n)\right]\Delta t. \tag{3.53}$$

If there are two approximate characteristics that cross each other, the two characteristics will be computed in $M \geq 1$ discrete steps as follow: With $t^{n,m} = t^n + m\Delta t/M$, $m = M, M-1, \ldots, 1$, let

$$\begin{aligned}\bar{\mathbf{x}}^{n,m-1} = \bar{\mathbf{x}}^{n,m} - \frac{1}{2}&\left[u(\bar{\mathbf{x}}^{n,m}, t^{n,m}) + u(\bar{\mathbf{x}}^{n,m}\right.\\ &\left.- u(\bar{\mathbf{x}}^{n,m}, t^{n,m})\Delta t/M, t^{n,m-1})\right]\Delta t/M,\end{aligned} \tag{3.54}$$

$$\bar{\mathbf{x}}^{n,M} = \mathbf{x}. \tag{3.55}$$

If $\Delta t/M$ is small enough, the approximate characteristics do not cross each other.

Remark 3.4. For the advection diffusion problems (3.1)–(3.3), in the case of $\vec{u}\cdot\vec{\nu} < 0$ and $(K\nabla c)\cdot\vec{\nu} = 0$ on the part of boundary $\partial\Omega$, the "ghost cells" are required to construct the scheme near the boundary points. For example, for the left boundary $x = x_{1/2}$, the fourth order formulas of ghost cell values are (3.21)–(3.22) for cells $\Omega_{0,j}$ and $\Omega_{-1,j}$, and

$$C_{-2,j} = \frac{1}{11}\left(-54C_{3,j} + 195C_{2,j} - 130C_{1,j}\right), \tag{3.56}$$

$$C_{-3,j} = \frac{1}{11}\left(-130C_{3,j} + 456C_{2,j} - 315C_{1,j}\right) \tag{3.57}$$

for cells $\Omega_{-2,j}$ and $\Omega_{-3,j}$.

In the case of $\vec{u}\cdot\vec{\nu} < 0$ and the concentration Dirichlet boundary condition on the part of boundary $\partial\Omega$, the "ghost cells" can be used to construct the scheme near the boundary points. For example, if $c(x_{1/2}, y, t) = g_{in}(y,t)$ at the left boundary

$x = x_{1/2}$, the fourth order formulas of ghost cell values are

$$C_{0,j} = \frac{1}{3}\left(-13C_{1,j} + 5C_{2,j} - C_{3,j} + 12g_{in}(y,t)\right), \tag{3.58}$$

$$C_{-1,j} = \frac{1}{3}\left(-70C_{1,j} + 32C_{2,j} - 7C_{3,j} + 48g_{in}(y,t)\right), \tag{3.59}$$

$$C_{-2,j} = \frac{1}{3}\left(-190C_{1,j} + 95C_{2,j} - 22C_{3,j} + 120g_{in}(y,t)\right), \tag{3.60}$$

$$C_{-3,j} = \frac{1}{3}\left(-395C_{1,j} + 208C_{2,j} - 50C_{3,j} + 24g_{in}(y,t)\right) \tag{3.61}$$

for cells $\Omega_{0,j}$, $\Omega_{-1,j}$, $\Omega_{-2,j}$, and $\Omega_{-3,j}$.

Remark 3.5. The PPM interpolation used in the construction of the scheme here is fourth order for equally spaced grids as shown in [13, 60]. For nonuniform grids, the fourth order accuracy can be obtained by the piecewise quartic method (PQM) proposed by White and Adcroft [57].

Remark 3.6. When performing the computation of Stage 2, if the X_i Lagrangian strip curl (subdomain within Lagrangian lines $X_{i-\frac{1}{2}}$ and $X_{i+\frac{1}{2}}$) is rotated more than 90 degrees, the upper limit $\tilde{y}_{i,j+1/2}$ in (3.28) will be less than its lower limit $\tilde{y}_{i,j-1/2}$ for some backtracked region and may cause an incorrect integral result. In this case, time step size will be decreased to compute a new Lagrange mesh to avoid the problem.

4. Solving the atmospheric pollution advection diffusion system. Considering the atmospheric pollutant advection diffusion problems that involve the large spatial scaled transport and diffusion processes and the small particle size scaled aerosol dynamical and chemical processes, the operator splitting method is applied to solve the complex system in each time interval.

Let Δt be the time step size, and let $N_t = T/\Delta t$ be a total step number. Denote $t^n = n\Delta t$. During the time interval $(t^n, t^{n+1}]$, a temporal second order splitting method [16, 33] is used for solving the atmospheric pollution problem (2.1).

On one hand, the spatial scale of the equations is very large (kilometers), but the aerosol dynamics and chemical processes of the equations are in a very small scale (of particle size in μm), making them two-scaled problems. During the time step, we use the operator splitting method to solve the system. On the other hand, as the size of domains in the horizontal direction is usually set to be hundreds of kilometers or larger, while the size of its domains in the vertical direction is only 20 kilometers or less, the vertical diffusion effect in the vertical direction is much stronger than that in the horizontal direction. Thus, the operator splitting method is also used to split the horizontal and vertical advection and diffusion processes during the time step, where the mesh step size in the horizontal direction (large mesh step size) is usually set to tens of kilometers, but the vertical mesh step size (small mesh step size) ranges from tens of meters to 1–2 kilometers in the vertical direction.

The temporal second order splitting method is defined as

$$\mathbf{c}(t+\Delta t) = (e^{\frac{1}{2}\Delta t\mathcal{A}_1} e^{\frac{1}{2}\Delta t\mathcal{A}_2} e^{\Delta t\mathcal{A}_3} e^{\frac{1}{2}\Delta t\mathcal{A}_2} e^{\frac{1}{2}\Delta t\mathcal{A}_1})\mathbf{c}(t) + O(\Delta t^2), \tag{4.1}$$

where $\mathcal{A}_1$ represents the horizontal advection and diffusion process, $\mathcal{A}_2$ represents the vertical advection and diffusion process, and $\mathcal{A}_3$ represents the nonlinear source process $\mathcal{F}_{l,s}$.

The multistep algorithm of the temporal second order splitting algorithm of the atmospheric pollution diffusion system is described below.

Step 1. With c_l^n being the value at t^n, we solve the multicomponent horizontal advection diffusion process in the time interval $(t^n, t^{n+\frac{1}{2}}]$ by the proposed MC-T2S4-CFVM in 2D to give a mass-conservative temporal second order and spatial fourth order solution

$$\frac{\partial c_l}{\partial t} = -\nabla \cdot (\vec{u}_h c_l) + \nabla \cdot (K_h \nabla c_l), \qquad l = 1, 2, \ldots, s, \tag{4.2}$$

where the mesh step size in the horizontal direction (large mesh step size) is usually set to tens of kilometers. Let the solutions be $c_{l,hori}^{n+\frac{1}{2}}$, $l = 1, 2, \ldots, s$.

Step 2. Using $c_{l,hori}^{n+\frac{1}{2}}$ as the value at t^n, we solve the vertical advection and diffusion process over $(t^n, t^{n+\frac{1}{2}}]$ by the MC-T2S4-CFVM in 1D to get a mass-conservative temporal second order and spatial fourth order solution

$$\frac{\partial c_l}{\partial t} = -\frac{\partial (u_\eta c_l)}{\partial \eta} + \frac{\partial}{\partial \eta}\left(K_\eta \frac{\partial c_l}{\partial \eta}\right), \qquad l = 1, 2, \ldots, s, \tag{4.3}$$

where the vertical mesh step size (fine mesh step size) ranges from tens of meters to 1–2 kilometers in the vertical direction. The solutions are denoted by $c_{l,vert}^{n+\frac{1}{2}}$, $l = 1, 2, \ldots, s$.

Step 3. Letting $c_{l,vert}^{n+\frac{1}{2}}$ be the concentration value of species l at t^n, one solves the source terms of the emission process, the nonlinear aerosol chemical process, and the nonlinear aerosol dynamic processes (condensation, coagulation, and deposition) on the small particle size scale (μm) over $(t^n, t^{n+1}]$,

$$\frac{\partial c_l}{\partial t} = \mathcal{L}_{l,aero}(\vec{c}) + R_{l,chem}(\vec{c}) + E_{l,emis}, \tag{4.4}$$

where the modal method, the sectional method, the temporal second order finite element method, and the temporal second order finite element method and wavelet method can be used to solve the small particle size scaled nonlinear aerosol dynamics, while the chemical reaction, i.e., chemical mechanism that describes the reactions among a set of chemical reactants, can be solved by the ISORROPIA algorithm [44] and by the moving cut HDMR method [12]. More details can be found in Remark 4.1 as well as the emission data.

The solutions are denoted by $c_{l,sour}^{n+1}$.

Step 4. Using $c_{l,sour}^{n+1}$ as the value at $t^{n+\frac{1}{2}}$, we solve the vertical advection diffusion by the MC-T2S4-CFVM in 1D over $(t^{n+\frac{1}{2}}, t^{n+1}]$,

$$\frac{\partial c_l}{\partial t} = -\frac{\partial (u_\eta c_l)}{\partial \eta} + \frac{\partial}{\partial \eta}\left(K_\eta \frac{\partial c_l}{\partial \eta}\right), \qquad l = 1, 2, \ldots, s. \tag{4.5}$$

Let the solutions be $c_{l,vert}^{n+1}$, $l = 1, 2, \ldots, s$.

Step 5. With $c_{l,vert}^{n+1}$ being the value at $t^{n+\frac{1}{2}}$, we solve the horizontal advection diffusion process by the MC-T2S4-CFVM in 2D in the time interval $(t^{n+\frac{1}{2}}, t^{n+1}]$,

$$\frac{\partial c_l}{\partial t} = -\nabla \cdot (\vec{u}_h c_l) + \nabla \cdot (K_h \nabla c_l), \qquad l = 1, 2, \ldots, s. \tag{4.6}$$

Finally, the solutions at t^{n+1} are denoted by c_l^{n+1}, $l = 1, 2, \ldots, s$.

Steps 1–5 are repeated until the final time period, $t = T$.

Remark 4.1. At Steps 1 and 5, we use the proposed MC-T2S4-CFVM in 2D to solve the horizontal advection diffusion process, which gives a mass-conservative temporal second order and spatial fourth order solution, while at Steps 2 and 4 we also solve the vertical advection diffusion process by MC-T2S4-CFVM in 1D. One important advantage of our mass-conservative temporal second order spatial fourth order characteristic finite volume method is that it can use large time step sizes to get highly accurate solutions and to save computational cost.

Remark 4.2. At Step 3, the multicomponent aerosol dynamic process (2.3)–(2.5) is defined on the size scale (μm), which can be solved by modal methods [56], sectional methods [30], finite element methods [49, 37], and wavelet method [36], etc., and we obtain the pollutant particle distributions in particle size. The chemical reaction process, i.e., chemical mechanism that describes the reactions among a set of chemical reactants, can be solved by ISORROPIA [44], which calculates the composition and phase state of an ammonia-sulfate-nitrate-chloride-sodium-calcium-potassium-magnesium-water inorganic aerosol system in thermodynamic equilibrium with gas phase precursors by numerically solving equilibrium equations, and the chemical reaction process can also be solved by the moving cut HDMR method [12]. The amount of pollutants discharged into the atmosphere is processed by using emission inventories, such as the National Emissions Inventory (NEI) [53], the INTEX-B inventory [62], the SEAC4RS inventory [40], the Regional Emission inventory in ASia v2.1 (REAS) [32], or the Multi-resolution Emission Inventory for China (MEIC, http://meicmodel.org/). On the other hand, for the small size scale multicomponent nonlinear source processes, including aerosol dynamics, chemical reaction processes, and emission, the fine time step size can be further used in each time interval to get high accuracy in time.

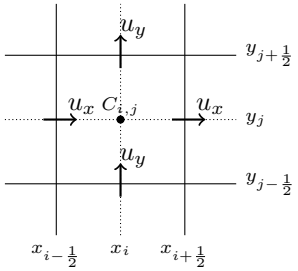

FIG. 3. *C-grid staggering.*

Remark 4.3. In MC-T2S4-CFVM combined with the computing velocity in atmospheric modeling, the spatial discretization uses C-grid staggering for the concentration and the velocity, where the concentration value $C_{i,j}$ represents cell-averaged concentration which can be considered a solved value at the center of a cell, while the velocity values are defined/solved at the middle points of the edges of a cell (see Figure 3).

5. Experimental results. In this section, we will first carry out numerical tests to observe the performance of our mass-conservative second order in time and fourth order in space characteristic finite volume method (MC-T2S4-CFVM) for solving 2D problems. The movement of a Gaussian pulse in two variable velocity fields is simulated by comparing it with the classical characteristic finite difference method [18]. A square with concentration 1 transporting in two different velocity fields is

tested by using MC-T2S4-CFVM. Then we show a local source emission transport test carried out in January 2016 and an air quality simulation in June 2016 in North China by our conservative MC-T2S4-CFVM methods.

5.1. Gaussian pulse movement in a 2D domain. We consider the advection diffusion problem (3.1) of a Gaussian concentration pulse moving in spatial domain $\Omega = [-1,1]\times[-1,1]$, with velocity $\vec{u} = (u_x, u_y) = (-4y, 4x)$. The initial concentration configuration of the Gaussian pulse is given by

$$c(x,y,0) = \exp\left(-\frac{(x-x_0)^2+(y-y_0)^2}{2\sigma_0^2}\right),\ (x,y)\in\Omega, \tag{5.1}$$

where $(x_0, y_0) = (-0.35, 0)$ is the initial center of the Gaussian pulse, and $\sigma_0 = 0.07$ is the standard deviation. The boundary condition is considered as a Neumann boundary condition obtained from the analytical exact solution, where the analytical exact solution is given as

$$c(x,y,t) = \frac{2\sigma^2}{2\sigma^2+4Kt}\exp\left(-\frac{(\bar{x}(t)-x_0)^2+(\bar{y}(t)-y_0)^2}{2\sigma^2+4Kt}\right), \tag{5.2}$$

with $\bar{x}(t) = x\cos(4t) + y\sin(4t)$ and $\bar{y}(t) = -x\sin(4t) + y\cos(4t)$. Numerical experiments are carried out using different diffusion coefficients of $K_x = K_y = K = 0, 10^{-5}$, respectively.

We first examine the convergence rates of numerical schemes in time by comparing the results at $T = \frac{\pi}{4}$ by different methods. Tables 1 and 2 exhibit the errors and ratios in time using different N_t by using our MC-T2S4-CFVM and a characteristic finite difference method based on bilinear interpolation (C-FDM-LI) and biquadratic interpolation (C-FDM-QI), with $K = 0$ and 10^{-5}, $\Delta x = \Delta y = \frac{1}{200}$, and $N_t = 20, 30, 40, 50$, and 60. The associated CFL numbers are 31.4, 20.9, 15.7, 12.6, and 10.5, respectively. We can see that our scheme gets second order accuracy in time for both the L_2 and L_∞ errors, while C-FDM-LI and C-FDM-QI get first order accuracy in time. The mass errors are also shown in the table, which indicates that MC-T2S4-CFVM preserves mass perfectly, while the mass errors for C-FDM-LI and C-FDM-QI are over 4×10^{-3}.

Now we test the convergence rates of numerical schemes in space. Tables 3 and 4 show the errors and ratios in space by using MC-T2S4-CFVM, C-FDM-LI, and C-FDM-QI with $\Delta t = 1/900$ and $\Delta x = \Delta y = \frac{1}{40}, \frac{1}{50}, \frac{1}{60}, \frac{1}{70}$, and $\frac{1}{80}$. Two different diffusion coefficients of $K = 0$ and $K = 10^{-5}$ are tested. We can see that the convergence rate of C-FDM-LI in space is less than one, C-FDM-QI gets second order accuracy in space, while our MC-T2S4-CFVM gets fourth order accuracy in space for both the L_∞ and L_2 errors. MC-T2S4-CFVM has much better performances. For example, when $K = 10^{-5}$, $h = 1/60$, the L_∞ and L_2 errors of C-FDM-LI are 6.7671×10^{-1} and 7.4585×10^{-2}, the errors of C-FDM-QI are 2.0311×10^{-1} and 2.2507×10^{-2}, while MC-T2S4-CFVM gets much smaller errors, 8.6210×10^{-3} and 8.2562×10^{-4}.

A group of plots at different times of $T = \pi/8, \pi/4, 3\pi/8$, and $\pi/2$, obtained by MC-T2S4-CFVM, C-FDM-LI, and C-FDM-QI, display the propagation of the moving Gaussian hump as shown in Figure 4. The diffusion coefficient is $K = 10^{-5}$. It is clear that MC-T2S4-CFVM simulates the surface of the Gaussian hump very well, while C-FDM-LI and C-FDM-QI smear the hump badly. Both C-FDM-LI and C-FDM-QI schemes deform the shape of the Gaussian hump, while our MC-T2S4-CFVM perfectly simulates the propagation of the Gaussian pulse and is in excellent agreement with the exact solution.

TABLE 1

Errors and ratios in time for the 2D advection diffusion problem using our MC-T2S4-CFVM and a characteristic finite difference method based on bilinear interpolation (C-FDM-LI) and biquadratic interpolation (C-FDM-QI), with $K = 0$, $\Delta x = \Delta y = \frac{1}{200}$, and $N_t = 20, 30, 40, 50,$ and 60.

	N_t	20	30	40	50	60
C-FDM-LI	E_∞	7.5524e-1	5.5418e-1	4.3127e-1	3.5187e-1	2.9891e-1
	Ratio	0.3919	0.7635	0.8717	0.9118	0.8945
	E_2	9.2136e-2	6.7457e-2	5.2578e-2	4.2931e-2	3.6264e-2
	Ratio	0.4881	0.7689	0.8662	0.9084	0.9257
	E_{mass}	1.1879e-2	8.5915e-3	6.7137e-3	5.5052e-3	4.6639e-3
C-FDM-QI	E_∞	7.5783e-1	5.5625e-1	4.3185e-1	3.5104e-1	2.9520e-1
	Ratio	0.3875	0.7627	0.8800	0.9285	0.9503
	E_2	9.2762e-2	6.8169e-2	5.3291e-2	4.3591e-2	3.6825e-2
	Ratio	0.4820	0.7598	0.8559	0.9004	0.9251
	E_{mass}	1.1879e-2	8.5915e-3	6.7137e-3	5.5052e-3	4.6639e-3
MC-T2S4	E_∞	4.0140e-2	1.7665e-2	9.9213e-3	6.3366e-3	4.4032e-3
-CFVM	Ratio	2.0447	2.0243	2.0054	2.0092	1.9965
	E_2	5.6734e-3	2.5198e-3	1.4171e-3	9.0690e-4	6.2978e-4
	Ratio	2.0038	2.0016	2.0007	2.0003	2.0001
	E_{mass}	1.7347e-17	3.8164e-17	5.2042e-17	5.2042e-17	3.4694e-18

TABLE 2

Errors and ratios in time for the 2D advection diffusion problem using our MC-T2S4-CFVM and a characteristic finite difference method based on bilinear interpolation (C-FDM-LI) and biquadratic interpolation (C-FDM-QI), with $K = 10^{-5}$, $\Delta x = \Delta y = \frac{1}{200}$, and $N_t = 20, 30, 40, 50,$ and 60.

	N_t	20	30	40	50	60
C-FDM-LI	E_∞	7.5196e-1	5.5174e-1	4.2933e-1	3.5032e-1	2.9762e-1
	Ratio	0.3933	0.7636	0.8720	0.9114	0.8942
	E_2	9.1862e-2	6.7254e-2	5.2421e-2	4.2804e-2	3.6158e-2
	Ratio	0.4886	0.7690	0.8661	0.9083	0.9255
	E_{mass}	1.1879e-2	8.5915e-3	6.7137e-3	5.5052e-3	4.6639e-3
C-FDM-QI	E_∞	7.5456e-1	5.5379e-1	4.2997e-1	3.4952e-1	2.9388e-1
	Ratio	0.3889	0.7630	0.8797	0.9284	0.9510
	E_2	9.2483e-2	6.7960e-2	5.3127e-2	4.3457e-2	3.6713e-2
	Ratio	0.4826	0.7599	0.8560	0.9003	0.9250
	E_{mass}	1.1879e-2	8.5915e-3	6.7137e-3	5.5052e-3	4.6639e-3
MC-T2S4	E_∞	4.0301e-2	1.7910e-2	1.0123e-2	6.5865e-3	4.6643e-3
-CFVM	Ratio	2.0363	2.0002	1.9832	1.9261	1.8927
	E_2	5.6613e-3	2.5160e-3	1.4165e-3	9.0833e-4	6.3289e-4
	Ratio	2.0033	2.0002	1.9968	1.9913	1.9817
	E_{mass}	2.4286e-17	1.4225e-16	1.7694e-16	2.7756e-17	4.2674e-16

We now compare the computational costs of our MC-T2S4-CFVM with the characteristic finite difference methods based on linear interpolation (C-FDM-LI) and quadratic interpolation (C-FDM-QI). With $\Delta t = h$, CPU results are listed in Table 5 for the problem with $K = 10^{-5}$ for reaching the same accuracy. As shown in Table 5, C-FDM-LI and C-FDM-QI need much more CPU computational time than MC-T2S4 to get the same accuracy. For example, to get precision of 5×10^{-2}, C-FDM-LI needs to use $h = 1/60$ and CPU time of 0.967 seconds, C-FDM-QI needs to use $h = 1/55$ and CPU time of 0.805 seconds, while our MC-T2S4-CFVM only needs $h = 1/11$ and much less CPU time of 0.223. To get a precision of 2×10^{-2}, C-FDM-LI and C-FDM-QI need CPU computational time of 37.552 and 19.521 seconds, while our

TABLE 3

Errors and ratios in space for the 2D advection diffusion problem using our MC-T2S4-CFVM and a characteristic finite difference method based on quadratic interpolation (C-FDM-QI) with $K = 0$, $\Delta t = 1/900$, *and* $\Delta x = \Delta y = \frac{1}{40}, \frac{1}{50}, \frac{1}{60}, \frac{1}{70}$, *and* $\frac{1}{80}$.

	h	$\frac{1}{40}$	$\frac{1}{50}$	$\frac{1}{60}$	$\frac{1}{70}$	$\frac{1}{80}$
C-FDM-LI	E_∞	7.4664e-1	7.1847e-1	6.7951e-1	6.4736e-1	6.1558e-1
	Ratio	-	0.1724	0.3057	0.3145	0.3770
	E_2	8.6446e-2	8.0231e-2	7.4796e-2	6.9995e-2	6.5715e-2
	Ratio	-	0.3344	0.3847	0.4304	0.4725
	E_{mass}	3.3835e-4	3.3628e-4	3.3589e-4	3.3581e-4	3.3579e-4
C-FDM-QI	E_∞	3.6468e-1	2.7535e-1	2.0459e-1	1.5596e-1	1.2139e-1
	Ratio	-	1.2591	1.6293	1.7605	1.8767
	E_2	4.4979e-2	3.1279e-2	2.2641e-2	1.7037e-2	1.3270e-2
	Ratio	-	1.6279	1.7727	1.8446	1.8712
	E_{mass}	3.3578e-4	3.3578e-4	3.3578e-4	3.3578e-4	3.3578e-4
MC-T2S4	E_∞	2.5066e-2	1.0326e-2	4.9727e-3	2.7285e-3	1.6304e-3
-CFVM	Ratio	-	3.9745	4.0077	3.8937	3.8560
	E_2	2.8210e-3	1.1559e-3	5.4796e-4	2.8845e-4	1.6481e-4
	Ratio	-	3.9985	4.0939	4.1627	4.1917
	E_{mass}	3.7630e-12	3.0073e-14	7.6397e-15	4.6421e-15	1.6473e-14

TABLE 4

Errors and ratios in space for the 2D advection diffusion problem using our MC-T2S4-CFVM and a characteristic finite difference method based on quadratic interpolation (C-FDM-QI) with $K = 10^{-5}$, $\Delta t = 1/900$, *and* $\Delta x = \Delta y = \frac{1}{40}, \frac{1}{50}, \frac{1}{60}, \frac{1}{70}$, *and* $\frac{1}{80}$.

	h	$\frac{1}{40}$	$\frac{1}{50}$	$\frac{1}{60}$	$\frac{1}{70}$	$\frac{1}{80}$
C-FDM-LI	E_∞	7.4380e-1	7.1558e-1	6.7671e-1	6.4459e-1	6.1289e-1
	Ratio	-	0.1733	0.3062	0.3155	0.3776
	E_2	8.6227e-2	8.0015e-2	7.4585e-2	6.9789e-2	6.5515e-2
	Ratio	-	0.3351	0.3854	0.4312	0.4733
	E_{mass}	3.3836e-4	3.3628e-4	3.3589e-4	3.3581e-4	3.3579e-4
C-FDM-QI	E_∞	3.6261e-1	2.7354e-1	2.0311e-1	1.5480e-1	1.2044e-1
	Ratio	-	1.2633	1.6328	1.7620	1.8797
	E_2	4.4746e-2	3.1102e-2	2.2507e-2	1.6934e-2	1.3190e-2
	Ratio	-	1.6300	1.7741	1.8454	1.8716
	E_{mass}	3.3578e-4	3.3578e-4	3.3578e-4	3.3578e-4	3.3578e-4
MC-T2S4	E_∞	4.2034e-2	1.7422e-2	8.6210e-3	4.6373e-3	2.8100e-3
-CFVM	Ratio	-	3.9470	3.8587	4.0224	3.7515
	E_2	4.1344e-3	1.7251e-3	8.2562e-4	4.3757e-4	2.5091e-4
	Ratio	-	3.9172	4.0417	4.1187	4.1650
	E_{mass}	9.1499e-12	6.3994e-14	1.1970e-15	2.9837e-15	1.1432e-14

MC-T2S4-CFVM spends only 0.567 seconds and gets more accurate numerical results. The advantage of our proposed scheme is more remarkable in reducing computational CPU time when high accuracy is desired.

5.2. Gaussian pulse moving in a vortex. In this part, the transport of a Gaussian hump in a vortex velocity field is considered. The velocity field is divergence free, $\vec{u} = (u_x, u_y) = (\psi_y, -\psi_x)$, where $\psi(x, y) = \frac{1}{2}\exp(\sin(\pi x))exp(\sin(\pi y))$ (Figure 5 (a)) over domain $\Omega = [0, 1] \times [0, 1]$.

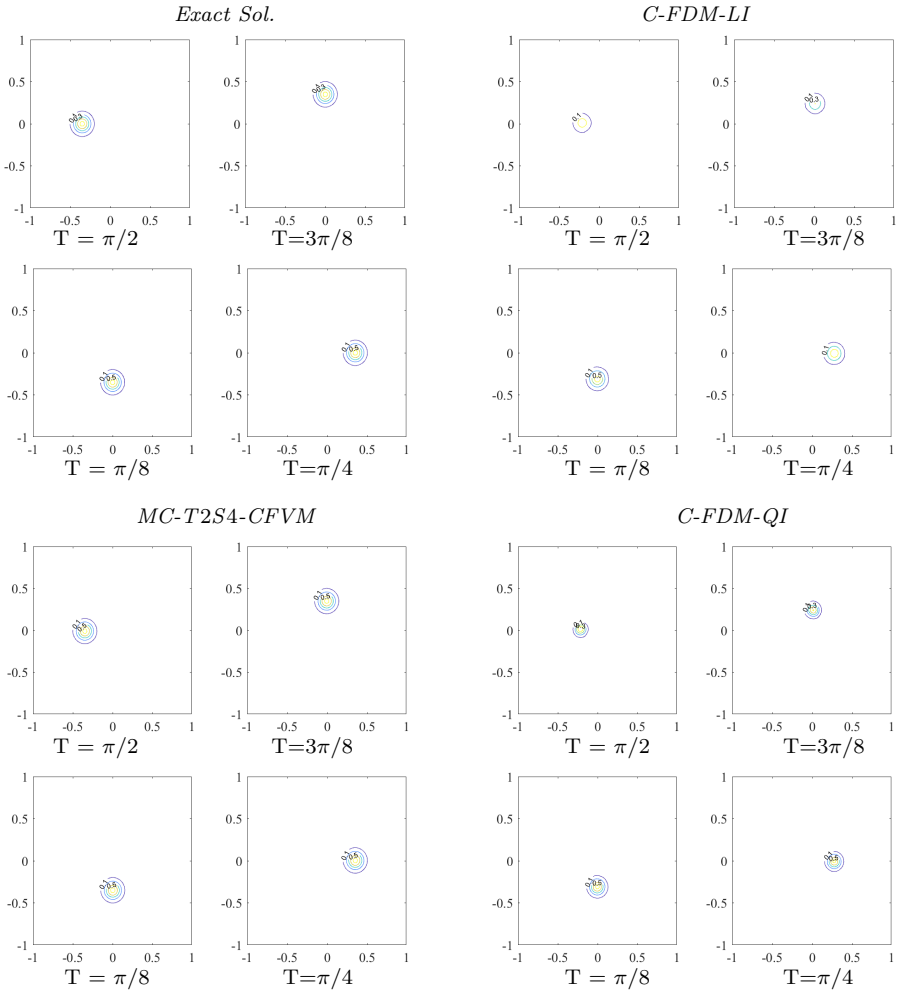

FIG. 4. *Comparison of the contour plots of the moving Gaussian hump in velocity field of* $(-4y, 4x)$ *at different times by different numerical methods, with exact solution as reference.*

TABLE 5

Computational cost comparison of our MC-T2S4-CFVM and the characteristic finite difference methods based on linear interpolation (C-FDM-LI) and quadratic interpolation (C-FDM-QI) for the problem with $K = 10^{-5}$ *and by* $\Delta t = h$.

C-FDM-LI			C-FDM-QI			MC-T2S4-CFVM		
E_2	h	CPU (s)	E_2	h	CPU (s)	E_2	h	CPU (s)
4.9732e-2	1/60	0.967	4.9814e-2	1/55	0.805	4.7073e-2	1/11	0.223
3.9954e-2	1/80	2.495	3.9816e-2	1/71	1.748	3.9367e-2	1/12	0.263
2.9901e-2	1/113	8.172	2.9758e-2	1/96	4.775	2.9924e-2	1/14	0.345
1.9985e-2	1/178	37.552	1.9888e-2	1/146	19.521	1.8884e-2	1/17	0.567

The initial distribution of the Gaussian hump is given as

$$c(x, y, 0) = \exp\left(-\frac{(x - x_0)^2 + (y - y_0)^2}{2\sigma_0^2}\right), \ (x, y) \in \Omega, \tag{5.3}$$

where the center of the initial Gaussian hump is specified as $x_0 = 0.75$ and $y_0 = 0.5$,

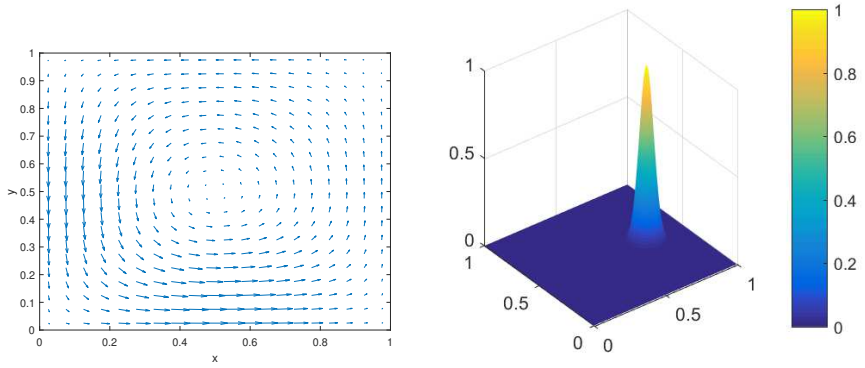

FIG. 5. (a) *Vortex velocity field of* $\vec{u} = (u_x, u_y) = (\psi_y, -\psi_x)$, *where* $\psi(x,y) = \frac{1}{2}\exp(\sin(\pi x))\exp(\sin(\pi y))$. (b) *Initial Gaussian pulse.*

as shown in Figure 5 (b). The source term is zero.

Taking the spatial step sizes $h_x = h_y = 1/100$ and the time step size $\Delta t = \frac{1}{40}$, a group of contour plots at time $T = 0$, $T = 0.25$, $T = 0.5$, and $T = 0.75$ are obtained using MC-T2S4-CFVM, C-FDM-LI, and C-FDM-QI and are presented in Figure 6. The distribution solved using a fine mesh of $h = \frac{1}{200}$ and $\Delta t = \frac{1}{200}$ is used as reference for the exact solution. We can see clearly that our method gets a perfect match with the exact solution, while C-FDM-LI and C-FDM-QI perform much worse, smearing the hump badly and losing a large area of the hump. Figure 7 displays the relative mass errors of the results computed by MC-T2S4-CFVM, C-FDM-LI, and C-FDM-QI as time increases. It can be seen that at time $T = 1$, C-FDM-LI and C-FDM-QI lose a majority percentage of the Gaussian hump mass, which is almost 70% at $T = 1$, while our MC-T2S4-CFVM conserves the mass perfectly.

5.3. Transporting a square of concentration 1. In this subsection, we test the transporting of a square with concentration 1 in two different velocity fields using MC-T2S4-CFVM.

We consider the transport problem without diffusion $K = 0$. The first velocity field is $\vec{u} = (u_x, u_y) = (1, 1)$ in 2D spatial domain $\Omega = [-1, 1] \times [-1, 1]$, and the initial concentration configuration is given by

$$c(x, y, 0) = \begin{cases} 1, & -0.5 \le x \le -0.3, -0.5 \le y \le -0.3, \\ 0 & \text{otherwise.} \end{cases} \tag{5.4}$$

The parameter values are $h = 1/100$, $T = 1$, and $N_t = 100$.

The second velocity field is $\vec{u} = (u_x, u_y) = (-4y, 4x)$ in 2D spatial domain $\Omega = [-1, 1] \times [-1, 1]$, and the initial concentration configuration is given by

$$c(x, y, 0) = \begin{cases} 1, & -0.1 \le x \le 0.1, 0.5 \le y \le 0.7, \\ 0 & \text{otherwise.} \end{cases} \tag{5.5}$$

The parameter values are $h = 1/100$, $T = \pi/2$ (one circle), and $N_t = 100$.

Computational results of the square of concentration 1 moving in the two velocity fields at different times are shown in Figure 8, where the contours are produced by using a level step of 0.01. With the first velocity, MC-T2S4-CFVM transports the square of concentration 1 from lower left to upper right, keeping its original shape and

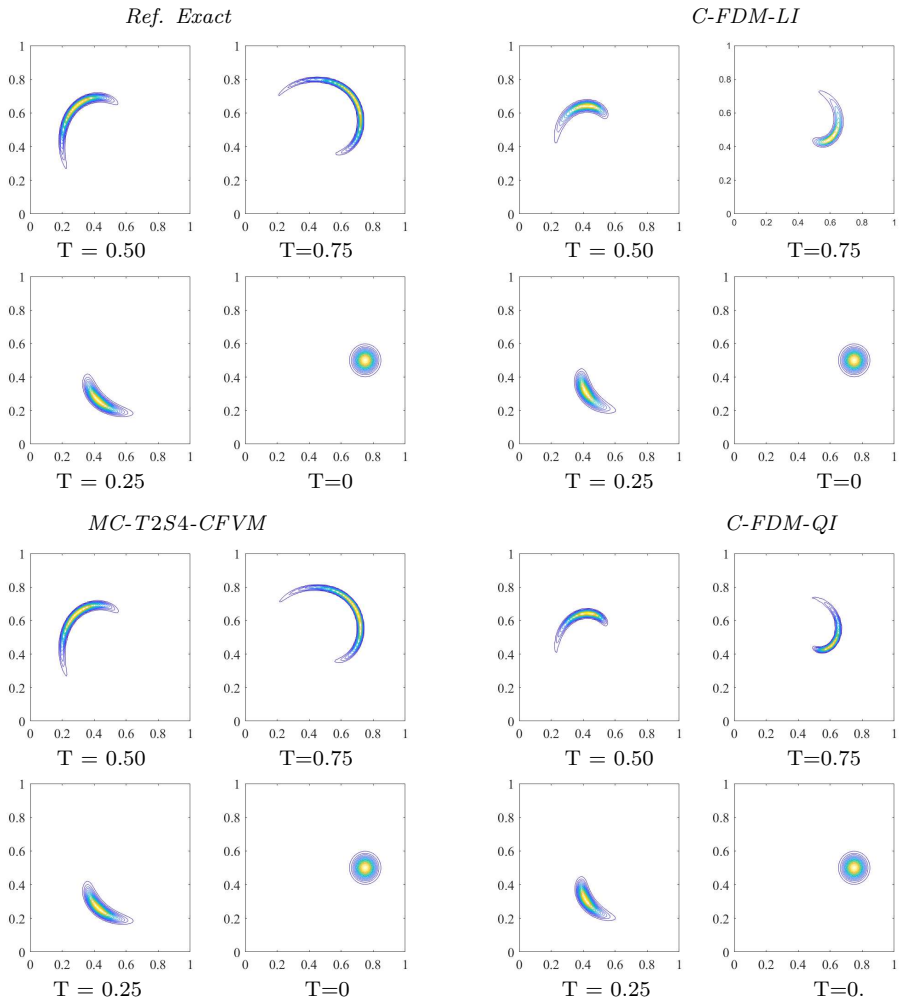

FIG. 6. *Comparison of the mesh plots of the moving Gaussian hump in a vortex at different times by different numerical methods, with exact solution given as reference.*

concentration 1 perfectly. In the second velocity field, our MC-T2S4-CFVM moves the square of concentration 1 rotating around the center of the domain, maintaining the shape and concentration 1 very well. These results exhibit that MC-T2S4-CFVM can conserve mass and volume when the more exact backtracked regions are used.

Remark 5.1. From this test of transporting a square of concentration 1, we can see that our MC-T2S4-CFVM can conserve mass and volume well. In our MC-T2S4-CFVM in section 3, the region $\bar{\Omega}_{i,j}(t^n)$ is a curved quadrilateral, backtracked from the cell $\Omega_{i,j}$ along the characteristics, which preserves volume. In real implementation, with the second order Runge–Kutta method (3.53) solving the characteristic line equation as pointed out in Remark 3.3 for our scheme, we can use multipoints on each edge of $\Omega_{i,j}$; then a more accurate backtracked $\bar{\Omega}_{i,j}(t^n)$ can be obtained, which will have the shape of a polygon and will provide a highly accurate backtracked region. We would like to mention that Arbogast and Huang [3] proposed a simple correction method stating that if a straight line is used, the midpoints of the cell edges can be

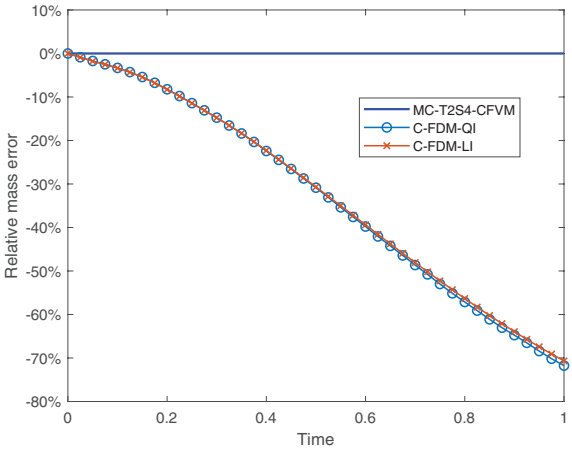

FIG. 7. *Time series of the relative mass error of the results computed by MC-T2S4-CFVM, C-FDM-LI, and C-FDM-QI when using a time step size of* $\Delta t = 1/50$ *and spatial step size of* $h_x = h_y = 1/100$.

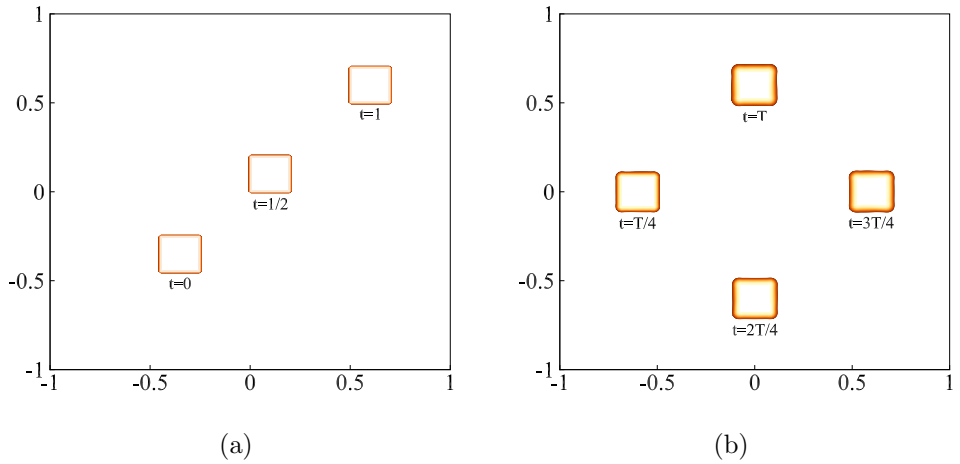

FIG. 8. *The contour figures of transporting a square of concentration* 1 *in two different velocity fields.*

used to get backtracked regions for improving volume accuracy.

5.4. Atmospheric pollution simulation. We now carry out realistic multicomponent atmospheric pollutant transport simulations for the Beijing–Tianjin–Hebei (BTH) region using the temporal second order splitting algorithm in section 4 where the proposed MC-T2S4-CFVMs solve the horizontal advection diffusion process at Steps 1 and 5 and the vertical advection diffusion process at Steps 2 and 4.

In implementation, the widely used WRF, a mesoscale numerical weather prediction system (WRF version 3, http://www2.mmm.ucar.edu/wrf/users/), is applied to generate the velocity field and other needed meteorological information, including wind components, temperature, pressure, water vapor, clouds, rainfall, etc. The

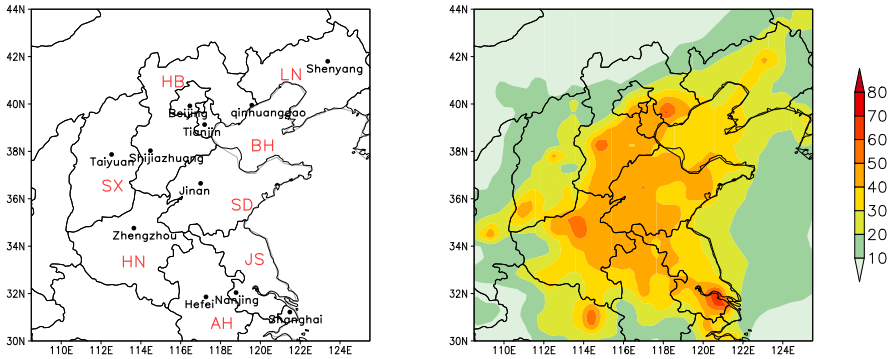

(a) (b)

FIG. 9. (a) *The modeling domain for North China. The locations of Hebei (HB), Shandong (SD), Jiangsu (JS), Anhui (AH), Zhejiang (ZJ), Henan (HN), Shanxi (SX), and Liaoning (LN) provinces, as well as the Bohai Sea (BH), are marked in red. The locations of Beijing, Tianjin, and Shanghai municipalities and the capitals of seven provinces are marked in black.* (b) *The spatial distribution of simulated averaged surface concentrations from* 10 *June to* 28 *June* 2016. *(Color available online.)*

WRF model produces numerical velocity based on actual atmospheric conditions from observations. We implement our time splitting algorithm—where MC-T2S4-CFVM in 2D solves the horizontal advection diffusion process and MC-T2S4-CFVM in 1D solves the vertical advection diffusion process—into the code of chemical transport model in WRF [24] (version 3), and the implemented MC-T2S4-CFVM system is then used to solve the multicomponent atmospheric pollutant transport simulation in the BTH region.

The studied domain (Figure 9 (a)) is a 1800 km × 1800 km area centered at (117° E, 37° N), which covers the three municipalities of Beijing, Shanghai, and Tianjin and the seven provinces in North China, including Hebei, Liaoning, Shanxi, Shandong, Henan, Jiangsu, and Anhui. The chosen domain is significant for the Beijing–Tianjin–Hebei (BTH) region, which is located in the North China Plain of mainland China, covers an area of 216,000 km^2 with a population exceeding 100 million. Because of the tremendously rapid urbanization and industrialization during the past few decades, the BTH region has become one of the most heavily polluted areas in the world due to the unprecedentedly high pollutant emissions. In addition to the emission and chemical formation, the air quality in BTH also largely depends on multiscale atmospheric circulations.

In the simulation of the multicomponent pollutant advection diffusions, the domain is divided into 36 × 36 grid cells with a spatial resolution of 50 km × 50 km for each cell. In the vertical direction, it has 30 vertical layers extending from the surface to the 100-hPa level (approximately 20 km); the vertical mesh interval ranges from 60 m near the ground to 1.5 km near the domain top. Both the meteorological information calculation (including velocity field) and pollutant transport simulation are carried out using the same mesh configuration.

With respect to the atmospheric chemistry configurations, the RADM2-MADE chemical mechanism [1, 24] is used. The initial value is set as low background value of concentration for each chemical species. On the inflow boundary, the Dirichlet boundary condition is provided with low background value of concentration, while on

the outflow boundary the Neumann boundary condition is applied. The anthropogenic emissions of CO, NOx, SO_2, NH_3, BC, OC, $PM_{2.5}$, and PM_{10} are set based on the monthly emission inventory [28, 38] with a resolution of 0.1 degree $\times$ 0.1 degree, which is the latest anthropogenic emissions data available for China (http://inventory.pku.edu.cn).

5.4.1. Local emission simulation. We first carry out a test experiment to investigate the local emission transport under the effect of East Asian monsoon winds during boreal winter in January 2016.

We assume there is only $PM_{2.5}$ emission at the location of Shijiazhuang city, which is one of the most polluted cities in China. The emission rate is from the Multi-resolution Emission Inventory for China (MEIC), and the emission rates at the other locations are set to zero. The simulation starts at 0000 UTC on 01 Jan. 2016, and runs for 10 days until 0000 UTC 11 Jan. 2016.

Figure 10 shows the spatial distribution of the simulated $PM_{2.5}$ concentrations at the ground level at different times. After one hour simulation from the start time, we can see from Figure 10 (a) that $PM_{2.5}$ mass concentration started to increase, but was at a low level of less than 50 μg m^{-3} and in a small area around the emission point. As time goes by, the concentration value increased gradually and reached a high value of over 100 μg m^{-3} at 1400 pm on 01 Jan. (Figure 10 (b)), and the polluted area enlarged at the same time.

Figures 10 (c)–(f) exhibit the impact of winds on pollutant transport. In January, the climate of much of mainland China is influenced by the East Asian monsoon, which causes the cold and dry winters and northeasterly winds because of the Siberian High. When the wind swept from northeast to southwest, as in Figure 10 (c), most of the area of Southern Hebei province and part of Shanxi province were influenced by the emitted $PM_{2.5}$ at Shijiazhuang. When the wind direction shifted to the west, large areas located to the east of Shijiazhuang, including the Tianjin region, were affected (Figure 10 (d)). When the wind direction shifted to the north and northwest, the $PM_{2.5}$ mass concentration in part of western and northern Shandong province reached 20–30 μg m^{-3} (Figures 10 (e)–(f)).

5.4.2. Realistic simulation. We then carry out a realistic simulation over the same domain. The emission information of pollutants from the MEIC is used. The simulations are initialized at 0000 UTC on 01 June 2016 and run for 4 weeks until 0000 UTC 29 June. The first 9 days are considered a spin-up period. And the atmospheric pollution episode selected for this study lasts from 10 June to 28 June 2016 Beijing Time (BJT = UTC + 8 h).

To validate the simulation results, the $PM_{2.5}$ mass concentration measurements are collected from air quality stations of the Chinese Ministry of Environmental Protection. The air quality stations scattered across seven provinces and the three municipalities of Beijing, Shanghai, and Tianjin could provide sufficient data to validate the model outputs.

The simulation results were first validated against the observations. Figure 11 compares the simulated and observed time series of $PM_{2.5}$ concentration in the three municipalities and the capitals of the seven provinces (the locations of the cities are marked in Figure 9 (a)). The diurnal variations of $PM_{2.5}$ concentration are generally well reproduced by the model. Figure 9 (b) presents the spatial distribution of simulated averaged surface concentrations from 10 June to 28 June 2016. From the observation data and the spatial distributions, it is clear that Shanghai, the largest city in the world, had significantly higher $PM_{2.5}$ concentrations in the simulated do-

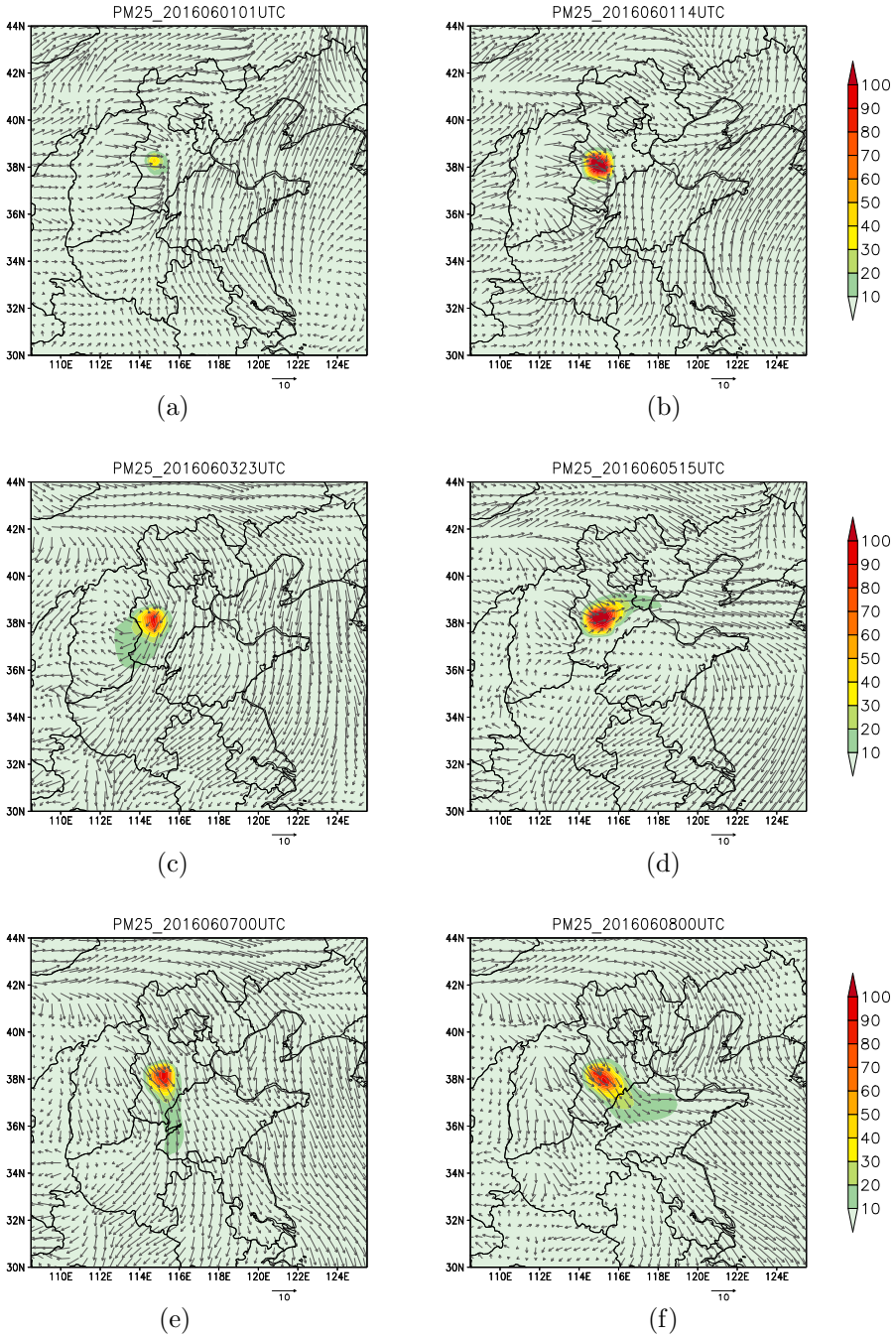

FIG. 10. *The spatial distribution of simulated ground level $PM_{2.5}$ concentrations in January* 2016.

main during that period. The other two municipalities of Beijing and Tianjin also suffered heavy pollution of $PM_{2.5}$.

Further, time series of simulated wind vector (direction and speed, taken at six-hour intervals) in Qinhuangdao from 10 June to 28 June 2016 are presented in Fig-

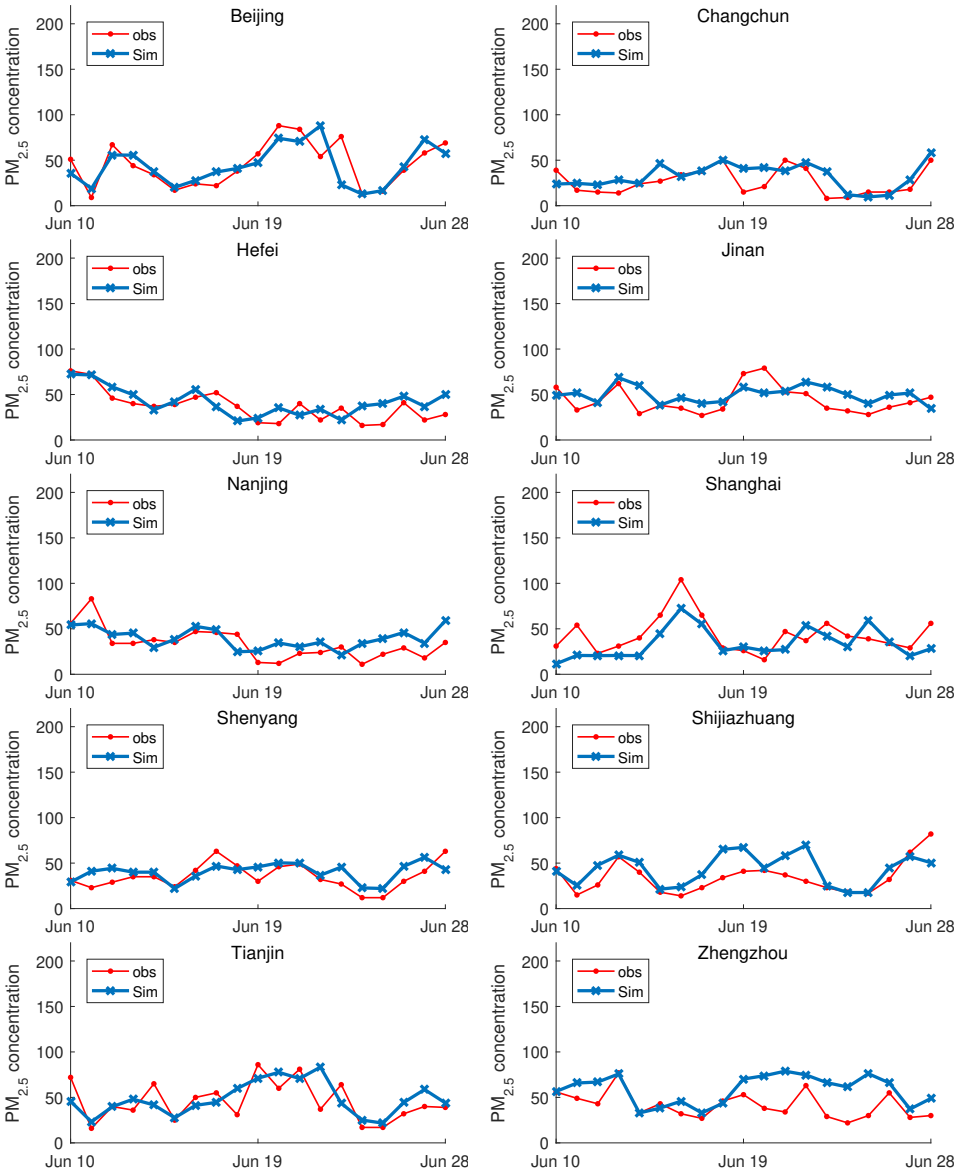

FIG. 11. *Comparisons of time series of simulated and observed daily average $PM_{2.5}$ concentration in the cities.*

ure 12. From the corresponding results in Figure 12, we can see that there were obvious impacts of wind conditions on the air quality. The high concentrations were all associated with the northerly winds, and winds from the south decreased the pollution. From 13 June to 15 June, and from 24 June to 25 June, the time when the wind flowed mainly in a southerly direction, the PM concentrations were at a relatively low level. However, when there were significantly strong northerly winds from 17 June to 22 June and on 28 June, low concentrations of $PM_{2.5}$ can be observed on exactly the same dates in Figure 12.

As the spatial distribution of simulated near-surface $PM_{2.5}$ concentration in Fig-

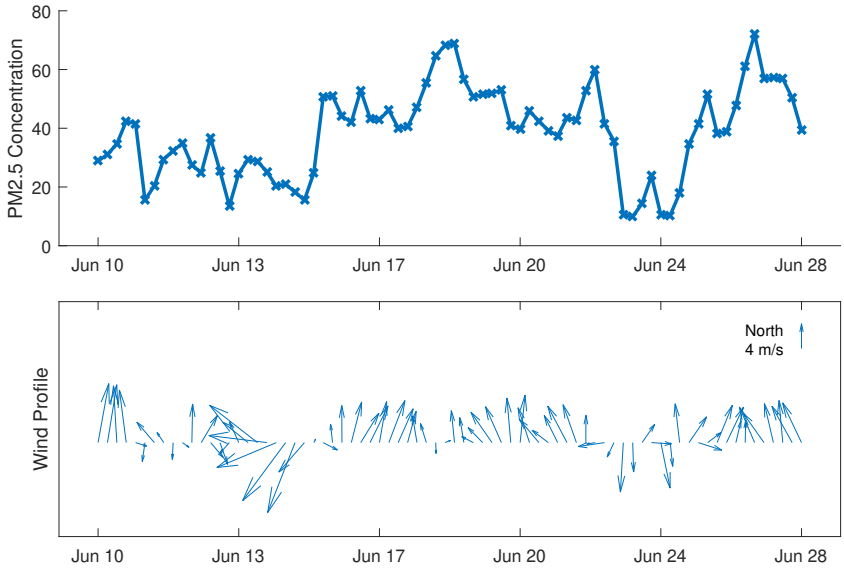

FIG. 12. *Time series of observed and simulated daily $PM_{2.5}$ concentrations and wind vector (direction and speed) in Qinhuangdao.*

ure 13 shows, at 1800 UTC 26 June, heavy pollutant loadings were found north of Jiangsu province, west of Shandong province, and south of the Hebei region. Southerly winds dominated over Shandong and Jiangsu provinces from 1200 UTC 26 June to 0600 UTC 27 June. These southerly winds could have brought the pollutants from Shandong and Jiangsu provinces to the downwind regions (Figures 13 (c)–(d)), such as Hebei province and the Bohai Sea, and even to Liaoning province, which is on the north side of the Bohai Sea (Figures 13 (e)–(f)).

6. Conclusions. We developed a mass-preserving temporal second order and spatial fourth order characteristic finite volume method (MC-T2S4-CFVM) for atmospheric pollutant transport problems by combining with the temporal second order operator splitting method. In the method, the advective term is treated by a conservative integral and characteristic tracking method, and the diffusion term is treated by high order discrete fluxes, which satisfies the continuity on both the element boundary and the boundary of the tracked regions. The developed method ensures the mass-conservative property and high accuracy. The temporal second order characteristic method alleviates the CFL restriction and allows one to use large time step sizes to carry out high-accuracy simulations. Numerical experiments demonstrate the mass conservation, accuracy, and computational efficiency of the developed method. Numerical applications of MC-T2S4-CFVM in realistic simulation over Eastern China show the big impact of winds on $PM_{2.5}$ concentration distributions. The results show that MC-T2S4-CFVM can be applied to large scale realistic atmospheric pollution simulations.

In this work, MC-T2S4-CFVM is applied to solve the 2D advection and diffusion splitting processes in the temporal second order splitting algorithm to atmospheric transport problems. The idea of MC-T2S4-CFVM can also be extended to 3D problems directly by three-stage conservative interpolation and by constructing high order discrete fluxes in 3D for backtracked regions.

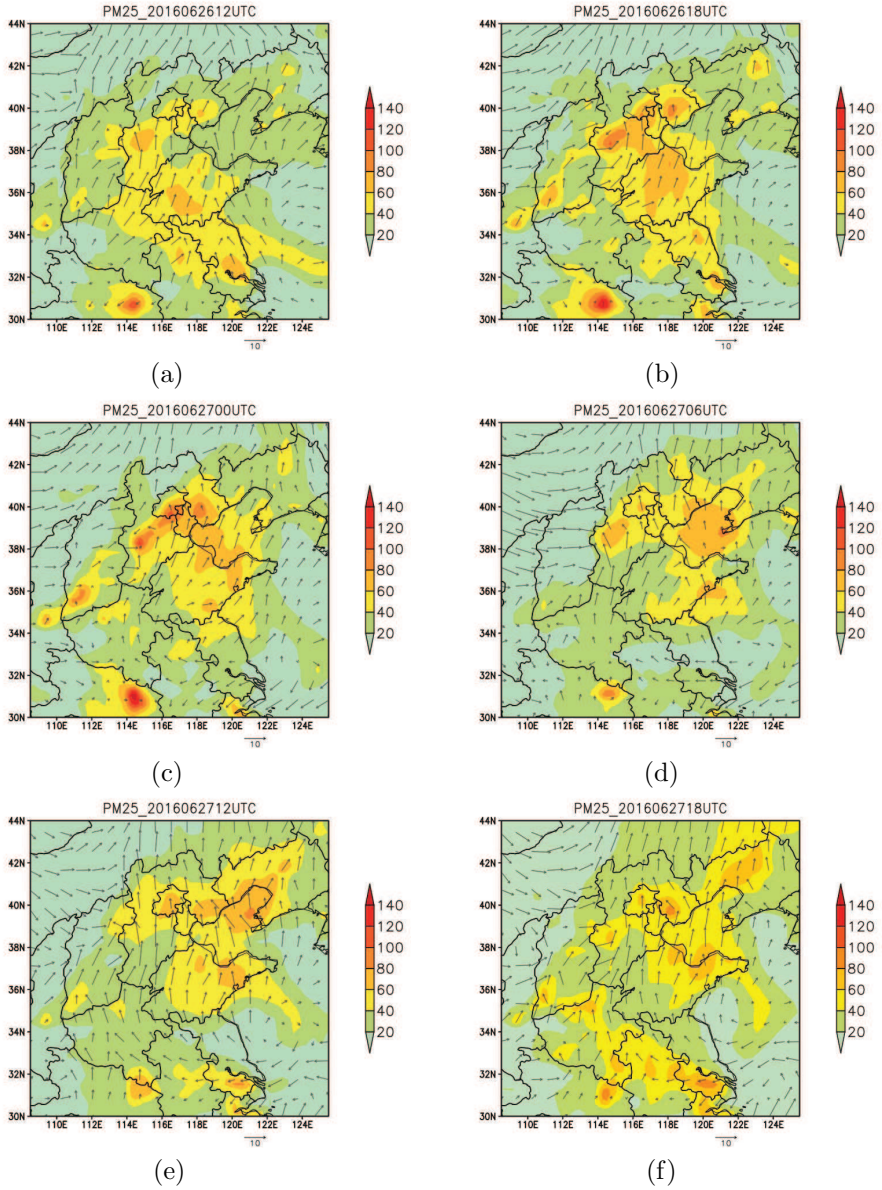

FIG. 13. *Spatial distribution of simulated averaged surface concentrations from* 1200*UTC* 26 *June to* 1800*UTC* 27 *June* 2016.

Acknowledgment. The authors would like to thank the reviewers for their valuable comments, which have helped to improve the paper greatly.

REFERENCES

[1] I. J. ACKERMANN, H. HASS, M. MEMMESHEIMER, A. EBEL, F. S. BINKOWSKI, AND U. SHANKAR, *Modal aerosol dynamics model for Europe: Development and first applications*, Atmospheric Environ., 32 (1998), pp. 2981–2999.

[2] T. ARBOGAST AND C. HUANG, *A fully conservative Eulerian-Lagrangian method for a*

convection-diffusion problem in a solenoidal field, J. Comput. Phys., 229 (2010), pp. 3415–3427.

[3] T. Arbogast and C.-S. Huang, *A fully mass and volume conserving implementation of a characteristic method for transport problems*, SIAM J. Sci. Comput., 28 (2006), pp. 2001–2022, https://doi.org/10.1137/040621077.

[4] T. Arbogast and M. F. Wheeler, *A characteristics-mixed finite element method for advection-dominated transport problems*, SIAM J. Numer. Anal., 32 (1995), pp. 404–424, https://doi.org/10.1137/0732017.

[5] U. M. Ascher, S. J. Ruuth, and B. T. R. Wetton, *Implicit-explicit methods for time-dependent partial differential equations*, SIAM J. Numer. Anal., 32 (1995), pp. 797–823, https://doi.org/10.1137/0732037.

[6] M. Bassett and J. H. Seinfeld, *Atmospheric equilibrium model of sulfate and nitrate aerosols*, Atmospheric Environ. (1967), 17 (1983), pp. 2237–2252.

[7] D. J. Benson, *An efficient, accurate, simple ALE method for nonlinear finite element programs*, Comput. Methods Appl. Mech. Engrg., 72 (1989), pp. 305–350.

[8] R. Bermejo, *A Galerkin-characteristic algorithm for transport-diffusion equations*, SIAM J. Numer. Anal., 32 (1995), pp. 425–454, https://doi.org/10.1137/0732018.

[9] M. Caputo, M. Giménez, and M. Schlamp, *Intercomparison of atmospheric dispersion models*, Atmospheric Environ., 37 (2003), pp. 2435–2449.

[10] M. A. Celia, T. F. Russell, I. Herrera, and R. E. Ewing, *An Eulerian-Lagrangian localized adjoint method for the advection-diffusion equation*, Adv. Water Resources, 13 (1990), pp. 187–206.

[11] E. Celledoni and B. K. Kometa, *Semi-Lagrangian Runge-Kutta exponential integrators for convection dominated problems*, J. Sci. Comput., 41 (2009), pp. 139–164.

[12] Y. Cheng, D. Liang, W. Wang, S. Gong, and M. Xue, *An efficient approach of aerosol thermodynamic equilibrium predictions by the HDMR method*, Atmospheric Environ., 44 (2010), pp. 1321–1330.

[13] P. Colella and P. R. Woodward, *The piecewise parabolic method (PPM) for gas-dynamical simulations*, J. Comput. Phys., 54 (1984), pp. 174–201.

[14] C. N. Dawson, T. F. Russell, and M. F. Wheeler, *Some improved error estimates for the modified method of characteristics*, SIAM J. Numer. Anal., 26 (1989), pp. 1487–1512, https://doi.org/10.1137/0726087.

[15] E. Debry and B. Sportisse, *Solving aerosol coagulation with size-binning methods*, Appl. Numer. Math., 57 (2007), pp. 1008–1020.

[16] I. Dimov, T. Ostromsky, and Z. Zlatev, *Challenges in using splitting techniques for large-scale environmental modeling*, in Advances in Air Pollution Modeling for Environmental Security, Springer, 2005, pp. 115–131.

[17] J. Donea, *Arbitrary Lagrangian-Eulerian finite element methods*, in Computational Methods for Transient Analysis, T. Belytschko and T. J. R. Hughes, eds., North-Holland, Amsterdam, 1983, pp. 474–516.

[18] J. Douglas, Jr., and T. F. Russell, *Numerical methods for convection-dominated diffusion problems based on combining the method of characteristics with finite element or finite difference procedures*, SIAM J. Numer. Anal., 19 (1982), pp. 871–885, https://doi.org/10.1137/0719063.

[19] R. E. Ewing, T. F. Russell, and M. F. Wheeler, *Convergence analysis of an approximation of miscible displacement in porous media by mixed finite elements and a modified method of characteristics*, Comput. Methods Appl. Mech. Engrg., 47 (1984), pp. 73–92.

[20] H. Flanders, *Differentiation under the integral sign*, Amer. Math. Monthly, 80 (1973), pp. 615–627.

[21] C. Fountoukis and A. Nenes, *ISORROPIA* II*: A computationally efficient thermodynamic equilibrium model for* K^+-Ca^{2+}-Mg^{2+}-NH_4^+-Na^+-SO_4^{2-}-NO_3^--Cl^--H_2O *aerosols*, Atmospheric Chem. Phys., 7 (2007), pp. 4639–4659.

[22] S. K. Friedlander, *Smoke, Dust, and Haze: Fundamentals of Aerosol Dynamics*, Topics in Chemical Engineering, Oxford University Press, 2000.

[23] T. M. Gaydos, R. Pinder, B. Koo, K. M. Fahey, G. Yarwood, and S. N. Pandis, *Development and application of a three-dimensional aerosol chemical transport model, PMCAMx*, Atmospheric Environ., 41 (2007), pp. 2594–2611.

[24] G. A. Grell, S. E. Peckham, R. Schmitz, S. A. McKeen, G. Frost, W. C. Skamarock, and B. Eder, *Fully coupled "online" chemistry within the WRF model*, Atmospheric Environ., 39 (2005), pp. 6957–6975.

[25] P. Hansbo, *The characteristic streamline diffusion method for convection-diffusion problems*, Comput. Methods Appl. Mech. Engrg., 96 (1992), pp. 239–253.

[26] C. W. Hirt, A. A. Amsden, and J. Cook, *An arbitrary Lagrangian-Eulerian computing method for all flow speeds*, J. Comput. Phys., 14 (1974), pp. 227–253.

[27] C.-S. Huang, T. Arbogast, and J. Qiu, *An Eulerian–Lagrangian WENO finite volume scheme for advection problems*, J. Comput. Phys., 231 (2012), pp. 4028–4052.

[28] Y. Huang, H. Shen, H. Chen, R. Wang, Y. Zhang, S. Su, Y. Chen, N. Lin, S. Zhuo, and Q. Zhong, *Quantification of global primary emissions of $PM_{2.5}$, PM_{10}, and TSP from combustion and industrial process sources*, Environ. Sci. Technol., 48 (2014), pp. 13834–13843.

[29] R. Kamakoti and C. Pantano, *High-order narrow stencil finite-difference approximations of second-order derivatives involving variable coefficients*, SIAM J. Sci. Comput., 31 (2009), pp. 4222–4243, https://doi.org/10.1137/080740829.

[30] Y. P. Kim and J. H. Seinfeld, *Simulation of multicomponent aerosol condensation by the moving sectional method*, J. Colloid Interface Sci., 135 (1990), pp. 185–199.

[31] O. Krüger and H. Grassl, *The indirect aerosol effect over Europe*, Geophys. Res. Lett., 29 (2002), pp. 31–1.

[32] J. Kurokawa, T. Ohara, T. Morikawa, S. Hanayama, G. Janssens-Maenhout, T. Fukui, K. Kawashima, and H. Akimoto, *Emissions of air pollutants and greenhouse gases over Asian regions during* 2000–2008*: Regional Emission inventory in ASia (REAS) version* 2, Atmospheric Chem. Phys., 13 (2013), pp. 11019–11058.

[33] D. Lanser and J. G. Verwer, *Analysis of operator splitting for advection–diffusion–reaction problems from air pollution modelling*, J. Comput. Appl. Math., 111 (1999), pp. 201–216.

[34] D. Liang, *A characteristics mixed finite element method of numerical simulation for* 2*-phase immiscible flows*, Sci. China Ser. A, 34 (1991), pp. 1281–1289.

[35] D. Liang, K. Fu, and W. Wang, *Modelling multi-component aerosol transport problems by the efficient splitting characteristic method*, Atmos. Environ., 144 (2016), pp. 297–314.

[36] D. Liang, Q. Guo, and S. Gong, *A new splitting wavelet method for solving the general aerosol dynamics equation*, J. Aerosol Sci., 39 (2008), pp. 467–487.

[37] D. Liang, W. Wang, and Y. Cheng, *An efficient second-order characteristic finite element method for non-linear aerosol dynamic equations*, Internat. J. Numer. Methods Engrg., 80 (2009), pp. 338–354.

[38] Z. Liu, D. Guan, W. Wei, S. J. Davis, P. Ciais, J. Bai, S. Peng, Q. Zhang, K. Hubacek, and G. Marland, *Reduced carbon emission estimates from fossil fuel combustion and cement production in China*, Nature, 524 (2015), pp. 335–338.

[39] I. Lomtev, R. Kirby, and G. Karniadakis, *A discontinuous Galerkin ALE method for compressible viscous flows in moving domains*, J. Comput. Phys., 155 (1999), pp. 128–159.

[40] Z. Lu and D. Streets, *The Southeast Asia Composition, Cloud, Climate Coupling Regional Study Emission Inventory*, 2012, http://bio.cgrer.uiowa.edu/SEAC4RS/html.

[41] A. Lundberg, P. Sun, C. Wang, and C.-S. Zhang, *Distributed Lagrange multiplier/fictitious domain finite element method for a transient Stokes interface problem with jump coefficients*, Comput. Model. Engrg. Sci., 119 (2019), pp. 35–62.

[42] R. D. Nair, J. S. Scroggs, and F. H. Semazzi, *Efficient conservative global transport schemes for climate and atmospheric chemistry models*, Monthly Weather Rev., 130 (2002), pp. 2059–2073.

[43] R. D. Nair, J. S. Scroggs, and F. H. M. Semazzi, *A forward-trajectory global semi-Lagrangian transport scheme*, J. Comput. Phys., 190 (2003), pp. 275–294.

[44] A. Nenes, S. N. Pandis, and C. Pilinis, *ISORROPIA: A new thermodynamic equilibrium model for multiphase multicomponent inorganic aerosols*, Aquatic Geochem., 4 (1998), pp. 123–152.

[45] C. Pilinis, *Derivation and numerical solution of the species mass distribution equations for multicomponent particulate systems*, Atmospheric Environment. Part A. General Topics, 24 (1990), pp. 1923–1928.

[46] J.-M. Qiu and A. Christlieb, *A conservative high order semi-Lagrangian WENO method for the Vlasov equation*, J. Comput. Phys., 229 (2010), pp. 1130–1149.

[47] J.-M. Qiu and C.-W. Shu, *Conservative high order semi-Lagrangian finite difference WENO methods for advection in incompressible flow*, J. Comput. Phys., 230 (2011), pp. 863–889.

[48] H. Rui and M. Tabata, *A mass-conservative characteristic finite element scheme for convection-diffusion problems*, J. Sci. Comput., 43 (2010), pp. 416–432.

[49] A. Sandu, *Piecewise polynomial solutions of aerosol dynamic equation*, Aerosol Sci. Technol., 40 (2006), pp. 261–273.

[50] J. H. Seinfeld and S. N. Pandis, *Atmospheric Chemistry and Physics: From Air Pollution to Climate Change*, John Wiley & Sons, 2012.

[51] B. Sportisse, *A review of current issues in air pollution modeling and simulation*, Comput.

Geosci., 11 (2007), pp. 159–181.
[52] J. M. Stockie, *The mathematics of atmospheric dispersion modeling*, SIAM Rev., 53 (2011), pp. 349–372, https://doi.org/10.1137/10080991X.
[53] U.S. Environmental Protection Agency, 2008 *National Emissions Inventory: Review, Analysis and Highlights*, https://www.epa.gov/sites/production/files/2015-07/documents/2008report.pdf, 2008.
[54] H. Wang, D. Liang, R. E. Ewing, S. L. Lyons, and G. Qin, *An approximation to miscible fluid flows in porous media with point sources and sinks by an Eulerian–Lagrangian localized adjoint method and mixed finite element methods*, SIAM J. Sci. Comput., 22 (2000), pp. 561–581, https://doi.org/10.1137/S1064827598349215.
[55] J. Wang, Z. Si, and W. Sun, *A new error analysis of characteristics-mixed FEMs for miscible displacement in porous media*, SIAM J. Numer. Anal., 52 (2014), pp. 3000–3020, https://doi.org/10.1137/130939717.
[56] E. R. Whitby and P. H. McMurry, *Modal aerosol dynamics modeling*, Aerosol Sci. Technol., 27 (1997), pp. 673–688.
[57] L. White and A. Adcroft, *A high-order finite volume remapping scheme for nonuniform grids: The piecewise quartic method (PQM)*, J. Comput. Phys., 227 (2008), pp. 7394–7422.
[58] K. Yang, P. Sun, L. Wang, J. Xu, and L. Zhang, *Modeling and simulations for fluid and rotating structure interactions*, Comput. Methods Appl. Mech. Engrg., 311 (2016), pp. 788–814.
[59] M. Zerroukat and T. Allen, *A three-dimensional monotone and conservative semi-Lagrangian scheme (SLICE-3D) for transport problems*, Quart. J. Royal Meteorolog. Soc., 138 (2012), pp. 1640–1651.
[60] M. Zerroukat, N. Wood, and A. Staniforth, *The parabolic spline method (PSM) for conservative transport problems*, Internat. J. Numer. Methods Fluids, 51 (2006), pp. 1297–1318.
[61] M. Zerroukat, N. Wood, and A. Staniforth, *Application of the parabolic spline method (PSM) to a multi-dimensional conservative semi-Lagrangian transport scheme (SLICE)*, J. Comput. Phys., 225 (2007), pp. 935–948.
[62] Q. Zhang, D. G. Streets, G. R. Carmichael, K. He, H. Huo, A. Kannari, Z. Klimont, I. Park, S. Reddy, J. Fu et al., *Asian emissions in* 2006 *for the NASA INTEX-B mission*, Atmospheric Chem. Phys., 9 (2009), pp. 5131–5153.
[63] Y. Zhang, B. Pun, K. Vijayaraghavan, S.-Y. Wu, C. Seigneur, S. N. Pandis, M. Z. Jacobson, A. Nenes, and J. H. Seinfeld, *Development and application of the model of aerosol dynamics, reaction, ionization, and dissolution (MADRID)*, J. Geophys. Res. Atmos., 109 (2004), D01202.